Generation and Impacts of Whistler-mode Waves During Energetic Electron Injections in Jupiter's Outer Radiation Belt

Q. Ma[1,2], W. Li[2], X.-J. Zhang[3], J. Bortnik[1], X.-C. Shen[2], A. Daly[2], W. S. Kurth[4], B. H. Mauk[5], F. Allegrini[6,7], J. E. P. Connerney[8], F. Bagenal[9], and S. J. Bolton[6]

[1]Department of Atmospheric and Oceanic Sciences, University of California, Los Angeles, California, USA.

[2]Center for Space Physics, Boston University, Boston, Massachusetts, USA.

[3]Department of Physics, University of Texas at Dallas, Richardson, Texas, USA.

[4]Department of Physics and Astronomy, University of Iowa, Iowa City, Iowa, USA.

[5]Applied Physics Laboratory, Laurel, Maryland, USA.

[6]Southwest Research Institute, San Antonio, Texas, USA.

[7]Department of Physics and Astronomy, University of Texas at San Antonio, San Antonio, Texas, USA.

[8]NASA Goddard Space Flight Center, Greenbelt, Maryland, USA.

[9]Laboratory for Atmospheric and Space Physics, University of Colorado Boulder, Colorado, USA.

Corresponding author: Qianli Ma (qianlima@ucla.edu)

Key Points:

- Chorus wave generation due to electron injections is demonstrated by their correlative occurrence and wave instability analysis
- Whistler-mode waves scatter electrons into the loss cone and cause diffuse auroral precipitation with intensities of 60-160 erg/cm^2/s
- Chorus waves cause local acceleration of MeV electrons in several days, further aided by the seed electron population from injections

Abstract

Energetic particle injections are commonly observed in Jupiter's magnetosphere and have important impacts on the radiation belts. We evaluate the roles of electron injections in the dynamics of whistler-mode waves and relativistic electrons using Juno measurements and wave-particle interaction modeling. The Juno spacecraft observed injected electron flux bursts at energies up to 300 keV at M shell ~11 near the magnetic equator during perijove-31. The electron injections are related to chorus wave bursts at 0.05-0.5 f_{ce} frequencies, where f_{ce} is the electron gyrofrequency. The electron pitch angle distributions are anisotropic, peaking near 90° pitch angle, and the fluxes are high during injections. We calculate the whistler-mode wave growth rates using the observed electron distributions and linear theory. The frequency spectrum of the wave growth rate is consistent with that of the observed chorus magnetic intensity, suggesting that the observed electron injections provide free energy to generate whistler-mode chorus waves. We further use quasilinear theory to model the impacts of chorus waves on 0.1-10 MeV electrons. Our modeling shows that the chorus waves could cause the pitch angle scattering loss of electrons at <1 MeV energies and accelerate relativistic electrons at multiple MeV energies in Jupiter's outer radiation belt. The electron injections also provide an important seed population at several hundred keV energies to support the acceleration to higher energies. Our wave-particle interaction modeling demonstrates the energy flow from the electron injections to the relativistic electron population through the medium of whistler-mode waves in Jupiter's outer radiation belt.

1. Introduction

Planetary electron radiation belts are strongly affected by resonant interactions between electrons and whistler-mode waves (Horne and Thorne, 2003; Horne et al., 2008; Thorne, 1983). Whistler-mode waves are right-hand polarized electromagnetic emissions at frequencies below the electron gyrofrequency and are commonly observed in Jupiter's outer radiation belt (Li et al., 2020; Menietti et al., 2012, 2016, 2020). Energetic electrons with sufficient pitch angle anisotropy generate whistler-mode waves through cyclotron resonance (Gary et al., 2012; Liu et al., 2011). On the other hand, the whistler-mode waves scatter the energetic electrons into the loss cone to cause their precipitation into the upper atmosphere (Bhattacharya et al., 1997; Li et al., 2017, 2021) and accelerate relativistic electrons in the Jupiter's outer radiation belt (Ma et al., 2020a; Shprits et al., 2012; Woodfield et al., 2013). The wave-particle interaction processes could be quantified using quasilinear modeling for relatively long periods compared to single wave-particle interaction timescales (Nénon et al., 2017; Woodfield et al., 2014).

Energetic electron injections provide an important energy source for whistler-mode wave generation (Li et al., 2009a; Xiao et al., 2003). Electron injections are commonly observed in Jupiter's middle magnetosphere and are associated with the auroral structures equatorward of the main auroral oval (Dumont et al., 2018; Gray et al., 2017; Thorne and Tsurutani, 1979). The Galileo mission statistics show that injections have a high occurrence rate at $M < 12$ and occur across all local times (Mauk et al., 1999, 2002). Following the azimuthal drift motion of particles after injection, the lower energy electrons could be observed earlier than the higher energy electrons, thereby demonstrating an energy dispersion signature in spacecraft observations (Haggerty et al., 2019; Mauk et al., 2002). The pitch angle distribution of injected electrons is usually pancake-like, which is different from the field-aligned distributions at M shells higher than the injection region (Ma et al., 2021a; Tomás et al., 2004). The Earth's radiation belt modeling demonstrates that the injections provide both the source electrons for chorus wave generation and the seed electrons for acceleration (Jaynes et al., 2015), which are important for the rapid enhancement of relativistic electron fluxes during geomagnetic storms (Ma et al., 2018; Thorne et al., 2013). Energetic electron injections may play similar roles in Jupiter's outer radiation belt (Tao et al., 2011), which will be analyzed in this paper.

The Juno spacecraft (Bolton et al., 2010; Bagenal et al., 2017) has polar orbits around Jupiter and samples the region near the magnetic equator at $M < 15$ after the 20^{th} orbit in May 2019. Electron injections were observed at high magnetic latitudes during the early orbits (Haggerty et al., 2019). Because the local magnetic field is weaker at the equator and the high pitch angle electrons mirror within a narrow latitude range near the equator, the most efficient wave generation and wave-particle interaction processes occur at low magnetic latitudes. Juno's equatorial measurements of waves and particles are essential for performing a quantitative modeling during an injection event.

In this paper, we investigate the whistler-mode wave generation, energetic electron precipitation, and relativistic electron acceleration processes during an electron injection event observed by Juno near the equator. The Juno observations of whistler-mode waves and electrons, as well as the wave generation are presented in Section 2. We perform a quasilinear modeling of wave-particle interaction processes in Section 3. We summarize and discuss our results in Section 4.

2. Chorus wave generation by electron injections

2.1 Juno observations of whistler-mode waves and electrons

We analyze the Juno measurements of whistler-mode waves and electron fluxes near the magnetic equator during the perijove-31 (PJ-31) approach on 30 December 2020. The orbital period was about 53.5 days, and the spacecraft was at the magnetic local time of ~22 h before travelling to the polar region. The Juno magnetometer (MAG) provides the background magnetic field measurements in three orthogonal directions (Connerney et al., 2017), and the 1-s resolution data is used in this study. The Waves instrument provides the wave magnetic field (B_w) power at 50 Hz - 20 kHz frequencies and electric field (E_w) power at 50 Hz - 40 MHz frequencies with a time resolution of 1 s (Kurth et al., 2017). The ratio $E_w/(c \cdot B_w)$ is calculated after considering the electric dipole antenna length, where c is the speed of light. We use Jovian Auroral Distributions Experiment (JADE) (McComas et al., 2017) measurements to obtain the pitch angle and energy distributions of electron fluxes from ~50 eV to 30 keV. The electron count rate is converted to flux by considering the geometric factor in Allegrini et al. (2021). We use Jupiter Energetic Particle Detector Instrument (JEDI) (Mauk et al., 2017) measurements to obtain the pitch angle and energy distributions of electron fluxes from 30 keV to 1 MeV. The penetrating electron fluxes at 100-200 keV energies due to minimum ionizing artifacts are corrected following the procedure in Mauk et al. (2018). Jupiter's internal magnetic field model JRM-33 (Connerney et al., 2022a) and external current sheet model CON-2020 (Connerney et al., 2020) are used to calculate the M shell, map the measured local magnetic field to the magnetic equator, and obtain the magnetic field line geometry to be used in the quasilinear analysis.

Figure 1 shows the 6-hour observation of waves and electron fluxes, when Juno was travelling towards lower M shells passing through the magnetic equator at $9 < M < 11.5$ (Figure

1e). The wave magnetic power spectrogram shows bursty and intense chorus waves at $0.05f_{ce}$ - f_{ce} frequencies occurring during 11:28 - 13:05 UT (Figure 1b). Here f_{ce} is the electron gyrofrequency calculated using the local magnetic field measurement. Electron cyclotron harmonic waves were observed at frequencies above f_{ce} during 12:15 - 14:35 UT with the highest intensity in the first harmonic band (Figure 1a). During this period, the wave electric power measurements show an intensification of hiss waves at frequencies below $0.05f_{ce}$, and the magnetic power measurements show occasional bursts of hiss waves. After 14:35 UT, Juno travelled away from the equator, and observed chorus and hiss waves at frequencies above and below $0.05\,f_{ce}$, respectively. The chorus waves are less intense at $M < 9$ after 14:35 UT than the chorus waves observed at $M \sim 11$ during 11:28 - 12:35 UT. The frequency of major chorus wave power spectral densities roughly follows the variation of equatorial electron gyrofrequency, suggesting that the chorus waves are generated near the magnetic equator. The wave properties are similar to the observations near the equator in the previous studies (Li et al., 2020; Menietti et al., 2012, 2020, 2021).

The JEDI and JADE measurements show bursts of injected electron fluxes at energies from 100 eV to 300 keV during 11:00 - 13:20 UT (Figures 1c-d). After 13:20 UT, the electron fluxes are relatively stable at energies above 30 keV, showing a peak flux at $M \sim 8.1$ (~15:45 UT). In general, the high fluxes of energetic electrons are observed during the same period when the chorus waves are observed.

We select the period of 11:59 - 12:34 UT to analyze the relation between chorus wave bursts and electron injections. This period is chosen because the spacecraft was close to the magnetic equator, strong intensities of whistler-mode waves were observed at frequencies above $0.05\,f_{ce}$, and both chorus wave bursts and electron injection bursts were observed together. The 35-min observation is presented in Figure 2.

Figure 2a shows wave electric power intensities at 30-50 kHz frequencies which are identified as upper hybrid emissions, in addition to the electron cyclotron harmonic (ECH) waves at lower frequencies. We estimated the upper hybrid resonance frequency (white dashed line) and calculated the total electron density. The average density is ~27.3 cm^{-3}, which is used as the density at the magnetic equator in the following modeling of wave generation and wave-particle interactions.

The wave electric power intensity, magnetic power intensity, and the ratio $E_w/(c{\cdot}B_w)$ are presented in Figures 2b-d. The chorus wave bursts are observed with the majority of their power in the $0.1\text{-}0.5f_{ce}$ frequency range, and the low $E_w/(c{\cdot}B_w)$ ratio suggests that the waves propagate close to the magnetic field direction based on cold plasma theory (Stix, 1992). At lower frequencies, the wave electric power shows an intensification of hiss waves, while the magnetic power shows several bursts of hiss waves, suggesting that the hiss may have both quasi-parallel and oblique wave components.

The energy spectrograms of electron flux and anisotropy at 1-300 keV energies are shown in Figures 2e-f. The enhancements of electron fluxes indicate electron injections with lower energy (e.g., 3-30 keV) electrons observed earlier than higher energy (e.g., 100-300 keV) electrons (Figure 2e). The energy dispersion is determined by the corotational electric field, as well as magnetic field gradient and curvature drifts (Mauk et al., 1999; Haggerty et al., 2019). Several chorus wave bursts are related to the injected electron bursts, although they do not appear simultaneously especially during later times. Using the measured pitch angle (α)

distribution of electron fluxes (j) at each energy (E), the electron anisotropy (A) is calculated as in Chen et al. (1999)

$$A(E) = \frac{\int_0^{\pi} j(\alpha,E)\sin^3\alpha d\alpha}{2\int_0^{\pi} j(\alpha,E)\cos^2\alpha\sin\alpha d\alpha} - 1 \tag{1}$$

The field-aligned, isotropic, and pancake pitch angle distributions correspond to negative, 0, and positive values of anisotropy, respectively. Figure 2f shows a transition from negative to positive anisotropies as energy increases to above 2 keV. The high anisotropy values are mainly observed at ~3-30 keV energies. Figure 2g shows the pancake pitch angle distributions measured at 10.9 keV energy, which is an example for the distributions with high anisotropy.

We calculate the electron minimum resonance energies for the chorus waves at $0.1f_{ce}$, $0.2f_{ce}$, and $0.5f_{ce}$ frequencies shown as the black dashed lines in Figures 2e-f. The calculation adopts 0° wave normal angle and 0° electron pitch angle, the measured total electron density and magnetic field, wave dispersion relation from cold plasma theory, and the cyclotron resonance condition. The energies of high anisotropy match the resonance energies of chorus waves. The electron anisotropy is higher at the times of injections than the anisotropy of background electron flux. The analysis of electron anisotropy provides evidence that the high electron fluxes with anisotropic pitch angle distribution at ~3-30 keV energies may generate the chorus waves at 0.1-$0.5f_{ce}$ frequencies.

Figure 2h shows the energy spectrogram of calculated wave growth rate using the observed electron phase space density distributions. The calculation details are presented in Section 2.2. The wave growth rates are high (>50 dB/R_J) when the injections provide both high fluxes and high pitch angle anisotropy; therefore, the simulated waves appear at the same time as the electron injections at 3-30 keV energies. The frequencies of high wave growth are mainly at ~500 Hz - 2 kHz, roughly consistent with the frequencies of the observed chorus waves. However, the observed chorus waves present a negative drift of wave frequency in the individual wave burst within ~2 min timescale (Figure 2c), which is not resolved in the simulated spectrogram of wave growth rate. The wave growth rate calculation shows overall high growth rates at high frequencies, obscuring the interpretation of frequency dispersion. It is also possible that the observed electrons were scattered by chorus waves and their pitch angle distributions changed from the initial injection that generated the waves.

2.2 Calculation of linear wave growth rates

Whistler-mode wave generation is simulated using the linear theory of wave instability (Kennel, 1966) and cold plasma dispersion. The local convective growth rate K_i is calculated as the integral of electron phase space density gradients under the resonance condition (Chen et al., 2010):

$$K_i = \sum_{n=-\infty}^{+\infty} \int_0^{\infty} dv_\perp \left(W_{\perp,n}\frac{\partial f}{\partial v_\perp} + W_{\parallel,n}\frac{\partial f}{\partial v_\parallel}\right)\Big|_{v_\parallel = v_{\parallel,res}} \tag{2}$$

where f is the phase space density, n is the resonance harmonic number, $v_\perp$ and $v_\parallel$ are the perpendicular and parallel particle velocities respectively, $W_{\perp,n}$ and $W_{\parallel,n}$ are the perpendicular and parallel weighting functions respectively. $v_\parallel$ is evaluated as the resonance velocity $v_{\parallel,res}$ satisfying the resonance condition:

$$\omega - k_\parallel v_{\parallel,res} = -n\Omega_{ce}/\gamma \tag{3}$$

where ω is the whistler-mode wave frequency, Ω_{ce} (defined as positive here) is the electron angular gyrofrequency, $k_{\parallel}$ is the parallel wave number, and γ is the relativistic factor. The resonant harmonic $n = -1$ provides the dominant contribution for the whistler-mode wave growth through cyclotron resonance. The analytical expressions of the weighting functions $W_{\perp,n}$ and $W_{\parallel,n}$ are provided in Kennel (1966).

As simulation inputs, our wave instability analysis model (Ma et al., 2014a) uses the satellite measurements of the particle flux distribution as a function of pitch angle and energy, total electron density, and total magnetic field. The wave growth rates are calculated for different wave normal angles and different wave frequencies along the satellite trajectory. This model has been used in our previous studies examining the whistler-mode and Z-mode wave generation during interchange instabilities at Jupiter (Daly et al., 2023), and magnetosonic wave generation in the Earth's inner magnetosphere (Ma et al., 2014a,b).

Figure 3 shows the wave growth rate calculation using Juno observations at ~12:00 UT on 30 December 2020. The electron fluxes measured by JADE and JEDI are averaged over 30 s after 12:08 UT, and converted into phase space density. The phase space density is plotted in the polar coordinate of electron energy and pitch angle in Figure 3a. The phase space densities are higher at ~90° pitch angle than those at ~0° or ~180°, suggesting an anisotropic distribution, which is typically unstable so that it would generate whistler-mode waves.

The wave growth rate is calculated as a function of wave frequency (ω/Ω_{ce}) and wave normal angle in Figure 3b. Since there is not a significant degree of asymmetry between the electron distributions near field-aligned and anti-field-aligned directions, we mirror the electron phase space densities relative to 90° pitch angle and calculate averages within the pitch angle ranges of 0°-90° and 90°-180°. The wave growth rate is shown only for the wave normal angles of 0°-30° since there is no positive wave growth for larger wave normal angles. The highest wave growth rate is found at ~0° wave normal angle due to cyclotron resonance, consistent with the observational evidence that the $E_w/(c \cdot B_w)$ ratio is low for chorus (Figure 2d). The calculated wave growth rate is compared with the observed chorus wave intensity as a function of wave frequency in Figure 2c. The agreement between the frequency spectra of the simulated wave growth and the observed wave intensity demonstrates that the observed electron distributions are unstable in the appropriate spectral range and provide the energy source for the chorus wave generation.

2.3 Rising-tone structures of chorus waves

Although the time cadence of the Waves instrument sampling is about 1 s during this event, rising-tone structures of chorus waves are nevertheless observed in the ~1-min wave spectrogram in Figure 4. The chorus wave elements show high electric and magnetic power densities, and $E_w/(c \cdot B_w) < 1$ suggesting quasi-parallel wave propagation. The chorus wave element frequency typically rises from $0.05f_{ce}$ to $0.5f_{ce}$ within a timescale of ~10 s. The chorus wave element may start in less than 5 s after the prior one, forming clusters of wave elements. The intensity gaps in the wave spectra found between different elements enable the identification of individual rising-tone structures. Comparing to the observations in Figure 2c, the collection of rising-tone wave elements forms the wave burst with an overall negative drifting frequency in ~2-min timescale.

The rising-tone structures shown in Figure 4 may be different from the typical rising-tone chorus waves observed in the Earth's radiation belts (Li et al., 2011). The rising-tone chorus waves in the Earth's radiation belts exhibit a faster frequency sweep rate and a shorter repetition period (less than 1 s) between different elements (Teng et al., 2017) than those shown in Figure 4. The variations within 1 s timescale cannot be resolved in Figure 4. However, the ~10 s rising-tone structures may imply the possible nonlinear wave-particle interactions in Jupiter's outer radiation belt, which is beyond the linear wave instability process discussed above.

2.4 Correlation between electron fluxes and ULF waves

Figure 2 shows electron flux bursts during injections in several minutes timescale. The observations in the Earth's outer radiation belt suggest that energetic electron fluxes could be correlated with ultra low frequency (ULF) waves, further modulating chorus wave generation and electron precipitation (Li et al., 2023; Rae et al., 2018; Xia et al., 2016; Zhang et al., 2019). We examine the relationship between magnetic field perturbations and electron fluxes in Jupiter's outer radiation belt using the 1-s magnetic field measurements by MAG instrument.

We subtract the total magnetic fields in 3 components by the smoothed magnetic fields over 10 min, and transform the magnetic fields into field-aligned coordinates to obtain the poloidal, toroidal, and compressional components as shown in Figure 5a. During this period, the local minima of compressional wave magnetic field are correlated with the high electron fluxes from ~1 keV to ~30 keV energy (Figure 5b), as indicated by the vertical dashed lines in Figure 5. Figure 5c compares the ~3.28 keV electron fluxes measured by JADE (blue) with the negative values of compressional wave magnetic field component (black). The high correlation shown in Figure 5c suggests that the electron fluxes are modulated by the compressional ULF waves. Similar to the coupling process reported in the Earth's radiation belts (Zhang et al., 2019), the perturbation in compressional magnetic field may lead to the radial transport of energetic electrons, since the electron phase space density increases with increasing M shell (Ma et al., 2021a). The modulated electron fluxes during the injection event further generate the chorus wave bursts on a timescale of a few minutes as shown in Figure 2.

3. Electron scattering and acceleration by whistler-mode waves

3.1 Calculation of diffusion coefficients

To analyze the electron scattering and acceleration by the observed whistler-mode waves during the injection event, we first use the Full Diffusion Code in Jupiter's radiation belts (Ma et al., 2020a) to calculate the bounce-averaged diffusion coefficients. The Full Diffusion Code requires the inputs of the frequency spectrum of wave magnetic intensity, total electron density, total background magnetic field, and wave normal angle distribution. The total electron density is obtained by identifying the upper hybrid frequency line (Figure 2a) and averaging over the period 11:59 - 12:34 UT. The latitudinal dependence of electron density is obtained from Dougherty et al. (2017) which is also used in Ma et al. (2020a), and the density is linearly scaled to match the observation at the equator (~27.3 cm^{-3}). The ratio between the plasma frequency and electron gyrofrequency at the equator is about 7.5.

We obtain the chorus wave frequency spectrum (shown as the black line in Figure 6) by selecting the waves at 0.05-0.5 f_{ce} frequencies and averaging the wave power density during 11:59 - 12:34 UT. The wave amplitude is found to be about 18 pT. The chorus waves are mainly quasi-field-aligned from the observation. The wave normal angle distribution is assumed to be a

Gaussian function in $X = \tan\theta$, such that the wave magnetic power is proportional to $\exp(-((X - X_m)/X_w)^2)$. We set the central wave normal angle as $X_m = 0$, wave normal width as $X_w = \tan 10°$, lower cutoff as $X_{LC} = 0$, and upper cutoff as $X_{UC} = \tan 30°$. The latitudinal range of the wave distribution is assumed to extend from the equator to 50° based on the previous statistical distribution of whistler-mode waves (Li et al., 2020). Based on our previous analysis about the latitudinal dependence of diffusion coefficients (Ma et al., 2020a), the chorus waves at latitudes below 20° play the major roles in multi-MeV electron acceleration and the precipitation at energies below 1 MeV.

The hiss wave frequency spectrum is obtained by selecting the waves at 50 Hz - 0.05 f_{ce} frequencies. Because the $E_w/(c \cdot B_w)$ of hiss presents two components with a ratio that is higher and lower than 1 respectively, we obtain the quasi-parallel hiss and oblique hiss waves by selecting the wave power densities with $E_w/(c \cdot B_w) < 1$ and $E_w/(c \cdot B_w) > 1$. The frequency spectra of the two components are shown as the blue and red lines in Figure 6, and the amplitudes are 9.4 pT and 4.2 pT, respectively. The total amplitude of chorus and hiss waves is similar to the statistical average amplitude of whistler-mode waves at $M \sim 10$ (Li et al., 2020). The wave normal angle and latitudinal distribution of quasi-parallel hiss waves are assumed to be the same as those of chorus waves. For oblique hiss waves, we assume that $X_m = \tan 65°$, $X_w = \tan 65°$, $X_{LC} = \tan 50°$, and $X_{UC} = \tan 80°$, and the latitudinal range extends from the equator to 10°.

The bounce-averaged pitch angle ($\langle D_{\alpha\alpha} \rangle$), momentum ($\langle D_{pp} \rangle$), and mixed pitch angle-momentum ($\langle D_{\alpha p} \rangle$) diffusion coefficients are presented in Figure 7. Here α is the pitch angle at the magnetic equator and p is the electron momentum. Since the energy of calculation is up to 30 MeV, we consider 50 orders of harmonic resonances ($-50 \le n \le 50$) to include all the possible scattering interactions. The chorus waves play the dominant role in the electron scattering at energies below 300 keV. Compared to $\langle D_{\alpha\alpha} \rangle$, the momentum diffusion due to chorus becomes important for energies above ~500 keV. The quasi-parallel hiss waves contriute to the scattering at energies above 100 keV and the scattering rates become comparable or higher than chorus at energies above 1 MeV. The electron scattering at >100 keV energies by oblique hiss waves is slower than quasi-parallel hiss. However, the oblique hiss waves cause more efficient Landau acceleration of electrons than chorus and quasi-parallel hiss waves, shown as the higher diffusion coefficients at low energies where $\langle D_{\alpha p} \rangle < 0$.

3.2 Modeling of electron precipitation by whistler-mode waves

We model the electron precipitation using the observed whistler-mode waves and electron fluxes along the Juno trajectory using the technique described in Ma et al. (2020b, 2021b). After the bounce-averaged pitch angle diffusion coefficients are calculated, the precipitation ratio, which is the ratio between the average electron flux inside the loss cone and the flux just outside the loss cone, is calculated as a function of energy by comparing $\langle D_{\alpha\alpha} \rangle$ at the loss cone ($\langle D_{\alpha\alpha} \rangle|_{LC}$) and the strong diffusion limit. The loss cone pitch angle is about 1° at the equator. It is assumed that the electron pitch angle distribution reaches a quasi-equilibrium state between pitch angle scattering from just outside the loss cone and precipitation loss inside the loss cone. The timescale to reach this quasi-equilibrium state is determined by the shorter time between the timescale of $\langle D_{\alpha\alpha} \rangle|_{LC}$ and the electron bounce period.

The modeling of electron precipitation by whistler-mode waves using quasilinear theory is shown in Figure 8. Figure 8a shows that the chorus wave amplitude reached 20-100 pT, quasi-field aligned hiss wave amplitude reached ~10-30 pT, and the oblique hiss wave amplitude was remained at a few pT. Figure 8b shows the $\langle D_{\alpha\alpha}\rangle|_{LC}$ due to both chorus and hiss waves. The electrons at ~1.5 keV - 100 keV energies are subject to the scattering near the loss cone on a timescale of a few hours, and the scattering rates become higher during wave bursts. The calculated precipitation ratio (Figure 8c) shows that the loss cone is nearly full (ratio greater than 0.8) at ~1.5-100 keV energies, while the loss cone at >100 keV energy is filled only when the whistler-mode chorus or hiss waves are strong. We obtain the electron fluxes just outside the loss cone from JADE and JEDI measurements (Figure 8d), and calculate the energy spectrogram of precipitating electron fluxes (Figure 8e) using the precipitation ratio. The total precipitating energy flux (Figure 8f) is calculated through the integral of the precipitating electron fluxes inside the loss cone (Ma et al., 2020b, 2021b). The total precipitating energy flux is found to be ~60-160 erg/cm^2/s during the injection event, which is a factor of ≳5 higher than the total precipitating energy flux during intense chorus wave events in the Earth's outer radiation belt (Ma et al., 2020b).

3.3 Modeling of local relativistic electron acceleration

The long-term electron phase space density evolution due to whistler-mode waves is modeled by performing 2D Fokker-Planck simulation at $M = 11$. We numerically solve the bounce-averaged Fokker-Planck equation (Ma et al., 2020a):

$$\frac{\partial f}{\partial t} = \frac{1}{T(\alpha)\sin\alpha\cos\alpha}\frac{\partial}{\partial\alpha}\left[T(\alpha)\sin\alpha\cos\alpha\left(\langle D_{\alpha\alpha}\rangle\frac{\partial f}{\partial\alpha} + p\langle D_{\alpha p}\rangle\frac{\partial f}{\partial p}\right)\right] + \frac{1}{p^2}\frac{\partial}{\partial p}(p^3\langle D_{\alpha p}\rangle\frac{\partial f}{\partial\alpha} + p^4\langle D_{pp}\rangle\frac{\partial f}{\partial p}) - \frac{f}{\tau} \quad (4)$$

where t is the time, $T(\alpha)$ is the normalized electron bounce period, and τ is a quarter of bounce period inside the loss cone and infinity outside the loss cone. We set $\frac{\partial f}{\partial\alpha} = 0$ at $\alpha = 0°$ and $\alpha = 90°$ as the low and high pitch angle boundary conditions, respectively. The low and high energy boundary conditions of phase space density are assumed to be constants at 30 keV and 30 MeV, respectively. The initial phase space density distribution is obtained from the 35-min average of Juno electron flux measurements. Since JEDI provides the electron flux up to 1 MeV energy, we assume that the electron phase space density decreases as a function of energy as a power law at energy above 1 MeV, i.e., $f \propto E^{-a}$ where a is obtained from the phase space density slope measured at the 700 keV - 1 MeV energy channels of JEDI. The simulation is performed for a 10-day timescale with a timestep of 1 s.

Figure 9a shows the simulated electron phase space density evolution due to chorus waves. The spin-averaged phase space density is plotted as a function of time and electron energy from 100 keV to 10 MeV. Due to the interaction with chorus waves, the phase space densities at energies below 1 MeV decrease due to the precipitation to the atmosphere, the electrons at 1-3 MeV energies are accelerated first and then their fluxes decay, and the electrons at >3 MeV energies are accelerated and remained at high levels during the 10-day period. The hiss waves, however, only cause gradual decay of electron fluxes at 100 keV - 1 MeV energies (Figure 9b). If both chorus and hiss waves are considered (Figure 9c), the electron flux decay at 200 keV - 3 MeV energies is faster than that due to chorus or hiss individually, while the electrons at >3 MeV energies are still accelerated and remain high over this period.

The Juno observations suggest that electron injections can provide high electron fluxes at energies up to 300 keV with anisotropic pitch angle distributions. These electron populations may also act as the seed electrons which are accelerated to energies above several MeV, similar to the roles of electron injections that play in the Earth's outer radiation belt (Allison et al., 2019). These seed electrons are not included in the simulations in Figures 9a-c. To demonstrate their effects on relativistic electron acceleration, we perform a simulation of electron scattering and acceleration due to chorus and hiss waves using a constant phase space density condition at 300 keV energy (Figure 9d). Compared to the results without seed electrons (Figure 9c), the electrons at 1-5 MeV energies are first accelerated and their phase space densities are stable afterwards. The simulation results at >5 MeV energies are similar between Figures 9c and 9d within the simulation period of 10 days, but their differences may be more significant for longer simulations (>10 days) due to the gradual development of differences at lower energies (< 5 MeV).

4. Conclusions and Discussions

We analyzed the resonant interaction processes that take place between electrons and whistler-mode waves during an electron injection event at $M \sim 11$. Juno observed bursts of injected electron fluxes and whistler-mode chorus and hiss waves near the magnetic equator. We calculated the wave growth rates to analyze the whistler-mode wave generation in association with electron injections, and used quasilinear modeling to quantify the energetic electron precipitation into Jupiter's atmosphere and relativistic electron acceleration by these same whistler-mode waves.

Our study is summarized with three major points for wave generation, electron precipitation, and relativistic electron acceleration, respectively.

- The electron injections provide high fluxes and high pitch angle anisotropies at >1 keV energies which act as the free energy source to generate whistler-mode chorus waves that are then observed by Juno. Local wave generation hypothesis is supported by the observations of electron injection bursts and chorus wave bursts, the pancake pitch angle distributions of energetic electrons, and the agreement between resonance energy of chorus and the unstable electron distributions. The wave generation is demonstrated through our linear wave growth rate calculation, which shows agreement between the frequency range of large positive wave growth rates and the observed chorus wave magnetic power density. The chorus wave power spectrogram shows rising-tone structures, suggesting possible nonlinear processes that take place in the chorus wave source.
- The whistler-mode waves could cause high precipitating energy flux of electrons from the equator to Jupiter's upper atmosphere during electron injections. The modeled total precipitating energy flux is 60-160 $erg/cm^2/s$, which is more than 5 times higher than that due to chorus waves during injections in the Earth's radiation belts (Ma et al., 2020b). The precipitation at >100 keV energies and the peaks of total precipitating energy flux are caused by strong chorus or hiss during the wave bursts. Chorus waves play a dominant role in the scattering loss of 1-100 keV electrons. At energies above 100 keV, hiss waves contribute comparably to chorus waves to electron scattering.
- The chorus waves are able to accelerate electrons at multiple MeV energies and cause the decay of lower energy electrons in Jupiter's outer radiation belt. The loss of <3 MeV electrons becomes faster when hiss wave scattering is also considered. Electron injections at energies up to 300 keV provide seed electrons, which could be accelerated to 1-3 MeV energies in less than 2 days and to 3-10 MeV energies over a longer period. The seed electron

fluxes are important for supporting a stable radiation belt intensity after the chorus-driven acceleration.

The roles of energetic electron injections in whistler-mode wave generation, diffuse auroral precipitation, and relativistic electron acceleration in Jupiter's outer radiation belt are qualitatively similar to those at the Earth (Li et al., 2009a; Jaynes et al., 2015; Thorne et al., 2013). However, there are also significant differences as discussed below.

Whistler-mode chorus and hiss waves are observed in the same region in Jupiter's outer radiation belt, while the chorus and hiss waves are mainly observed outside and inside the plasmapause in the Earth's radiation belts, respectively (Li et al., 2009b, 2015; Ma et al., 2023). The chorus waves at frequencies above 0.05 equatorial f_{ce} may be generated by the unstable injected electrons and are the major driver for the relativistic electron acceleration process. The hiss waves at lower frequencies may have mixed sources, such as propagation effects (Wang et al., 2008), and mainly drive electron flux decay.

The energetic electron precipitation at Jupiter is at least a factor of 5 higher than the precipitation at the Earth. The key factors leading to the more intense precipitation are the longer magnetic field line and higher level of trapped electron flux at Jupiter than those at the Earth. Our modeled precipitating energy flux is in the same order of magnitude as Juno's direct observation of the precipitating electrons, when the satellite was near the same M shells at high latitude close to Jupiter where the loss cone electron flux was resolved (Allegrini et al., 2020; Clark et al., 2018). The high precipitating energy flux may cause diffuse aurora phenomena in Jupiter's atmosphere (Li et al., 2017, 2021).

In our simulation, the timescale of multi-MeV electron acceleration by chorus at Jupiter is longer than the rapid acceleration of electrons in the Earth's radiation belts (Ma et al., 2018; Thorne et al., 2013). The chorus wave amplitude in our simulation is close to the statistical average, which is lower than the chorus wave amplitude during highly disturbed times in the Earth's radiation belts. At Jupiter, if higher amplitude chorus occurs under certain conditions, the acceleration timescale could be shorter than our simulation results; alternatively, if chorus waves with moderate amplitudes have a high occurrence rate, the chorus waves may persistently accelerate the electrons over a long time (Ma et al., 2020a; Woodfield et al., 2013). The frequent occurrence of electron injections at $M < 12$ (Mauk et al., 1999, 2002) may support the second scenario. Future studies are planned to reveal the properties of chorus and hiss waves and the efficiency of electron acceleration and precipitation on a global scale in the Jupiter's outer radiation belt.

Acknowledgments

We would like to acknowledge the NASA subcontract 699046X to UCLA and subcontract Q99064JAR to Boston University under prime contract ZZM06AA75C. This work was supported by the NASA grants 80NSSC20K0196, 80NSSC20K0557, and 80NSSC24K0572, and the NSF grants AGS-2021749 and AGS-2225445. The research conducted at the University of Iowa was supported by NASA through contract 699041X with the Southwest Research Institute.

Open Research

Data Availability Statement

The Juno data are retrieved from NASA Planetary Data System (https://pds-ppi.igpp.ucla.edu/mission/JUNO). Specifically, this study uses the Juno magnetometer data (Connerney, 2022b), JADE data (Allegrini et al., 2022), JEDI data (Mauk, 2022), Waves survey mode data (Kurth and Piker, 2022a), and Waves burst mode data (Kurth and Piker, 2022b). The simulation data in this study are available at the data repository https://doi.org/10.6084/m9.figshare.25347538 (Ma et al., 2024).

References

Allegrini, F., Mauk, B., Clark, G., Gladstone, G. R., Hue, V., Kurth, W. S., et al. (2020). Energy flux and characteristic energy of electrons over Jupiter's main auroral emission. *Journal of Geophysical Research: Space Physics, 125*, e2019JA027693. https://doi.org/10.1029/2019JA027693

Allegrini, F., Wilson, R. J., Ebert, R. W., and Loeffler, C. (2022), JUNO J/SW JOVIAN AURORAL DISTRIBUTION CALIBRATED V1.0, JNO-J/SW-JAD-3-CALIBRATED-V1.0 [Dataset], *NASA Planetary Data System*, doi:10.17189/1519715.

Allegrini, F., Kurth, W. S., Elliott, S. S., Saur, J., Livadiotis, G., Nicolaou, G., et al. (2021). Electron partial density and temperature over Jupiter's main auroral emission using Juno observations. *Journal of Geophysical Research: Space Physics, 126*, e2021JA029426. https://doi.org/10.1029/2021JA029426

Allison, H. J., Horne, R. B., Glauert, S. A., & Del Zanna, G. (2019). On the importance of gradients in the low-energy electron phase space density for relativistic electron acceleration. *Journal of Geophysical Research: Space Physics, 124*, 2628-2642. https://doi.org/10.1029/2019JA026516

Bagenal, F., A. Adriani, F. Allegrini, S. J. Bolton, B. Bonfond, E. J. Bunce, J. E. P. Connerney, S. W. H. Cowley, R. W. Ebert, G. R. Gladstone, C. J. Hansen, W. S. Kurth, S. M. Levin, B. H. Mauk, D. J. McComas, C. P. Paranicas, D. Santos-Costa, R. M. Thorne, P. Valek, J. H. Waite, and P. Zarka (2017), Magnetospheric Science Objectives of the Juno Mission, *Space Sci. Rev., 213*, 219-287, doi:10.1007/s11214-014-0036-8.

Bhattacharya, B., Thorne, R. M., Williams, D. J., Khurana, K. K., & Gurnett, D. A. (2005). Diffuse auroral precipitation in the Jovian upper atmosphere and magnetospheric electron flux variability. *Icarus, 178*(2), 406-416. https://doi.org/10.1016/j.icarus.2005.06.013

Bolton, S. J., and Juno Science Team (2010), The Juno mission, *Proc. Int. Astron. Union, 6* (S269), doi:10.1017/S1743921310007313.

Chen, M. W., J. L. Roeder, J. F. Fennell, L. R. Lyons, R. L. Lambour, and M. Schulz (1999), Proton ring current pitch angle distributions: Comparison of simulations with CRRES observations, *J. Geophys. Res., 104*(A8), 17,379-17,389.

Chen, L., R. M. Thorne, V. K. Jordanova and R. B. Horne (2010), Global simulation of magnetosonic wave instability in the storm time magnetosphere, *J. Geophy. Res., 115*, A11222, doi:10.1029/2010JA015707.

Clark, G., Tao, C., Mauk, B. H., Nichols, J., Saur, J., Bunce, E. J., Allegrini, F., Gladstone, R., Bagenal, F., Bolton, S., Bonfond, B., Connerney, J., Ebert, R. W., Gershman, D. J., Haggerty, D., Kimura, T., Kollmann, P., Kotsiaros, S., Kurth, W. S., Levin, S., McComas, D. J., Murakami, G., Paranicas, C., Rymer, A., & Valek, P. (2018). Precipitating electron energy flux and characteristic energies in Jupiter's main auroral region as measured by Juno/JEDI. *Journal of Geophysical Research: Space Physics, 123*, 7554-7567. https://doi.org/10.1029/2018JA025639

Connerney, J. E. P., M. Benn, J. B. Bjarno, et al. (2017), The Juno Magnetic Field Investigation. *Space Sci Rev., 213*, 39-138, https://doi.org/10.1007/s11214-017-0334-z.

Connerney, J. E. P., Timmins, S., Herceg, M., & Joergensen, J. L. (2020). A Jovian magnetodisc model for the Juno era. *Journal of Geophysical Research: Space Physics, 125*, e2020JA028138. https://doi.org/10.1029/2020JA028138

Connerney, J. E. P., Timmins, S., Oliversen, R. J., Espley, J. R., Joergensen, J. L., Kotsiaros, S., et al. (2022a). A new model of Jupiter's magnetic field at the completion of Juno's Prime Mission. *Journal of Geophysical Research: Planets, 127*, e2021JE007055. https://doi.org/10.1029/2021JE007055

Connerney, J. E. P. (2022b), Juno MAG CALIBRATED DATA J V1.0, JNO-J-3-FGM-CAL-V1.0 [Dataset], *NASA Planetary Data System*, https://doi.org/10.17189/1519711.

Daly, A., Li, W., Ma, Q., Shen, X.-C., Yoon, P. H., Menietti, J. D., et al. (2023). Plasma wave and particle dynamics during interchange events in the Jovian magnetosphere using Juno observations. *Geophysical Research Letters, 50*, e2023GL103894. https://doi.org/10.1029/2023GL103894

Dougherty, L. P., Bodisch, K. M., and Bagenal, F. (2017), Survey of Voyager plasma science ions at Jupiter: 2. Heavy ions, *J. Geophys. Res. Space Physics, 122*, 8257- 8276, doi:10.1002/2017JA024053.

Dumont, M., Grodent, D., Radioti, A., Bonfond, B., Roussos, E., & Paranicas, C. (2018). Evolution of the auroral signatures of Jupiter's magnetospheric injections. *Journal of Geophysical Research: Space Physics, 123*, 8489- 8501. https://doi.org/10.1029/2018JA025708

Gary, S. P., K. Liu, R. E. Denton, and S. Wu (2012), Whistler anisotropy instability with a cold electron component: Linear theory, *J. Geophys. Res., 117*, A07203, doi:10.1029/2012JA017631.

Gray, R. L., Badman, S. V., Woodfield, E. E., and Tao, C. (2017), Characterization of Jupiter's secondary auroral oval and its response to hot plasma injections, *J. Geophys. Res. Space Physics, 122*, 6415- 6429, doi:10.1002/2017JA024214.

Haggerty, D. K., Mauk, B. H., Paranicas, C. P., Clark, G., Kollmann, P., Rymer, A. M., et al. (2019). Jovian injections observed at high latitude. *Geophysical Research Letters, 46*, 9397- 9404. https://doi.org/10.1029/2019GL083442

Horne, R. B., and Thorne, R. M. (2003), Relativistic electron acceleration and precipitation during resonant interactions with whistler-mode chorus, *Geophys. Res. Lett., 30*, 1527, doi:10.1029/2003GL016973, 10.

Horne, R. B., R. M. Thorne, S. A. Glauert, J. D. Menietti, Y. Y. Shprits, and D. A. Gurnett (2008), Gyro-resonant electron acceleration at Jupiter, *Nature Physics, 4*, 301-304, doi:10.1038/nphys897.

Jaynes, A. N., et al. (2015), Source and seed populations for relativistic electrons: Their roles in radiation belt changes, *J. Geophys. Res. Space Physics, 120*, 7240-7254, doi:10.1002/2015JA021234.

Kennel, C. F. (1966), Low-Frequency Whistler Mode, *Physics of Fluids, 9*, 2190, doi:10.1063/1.1761588.

Kennel, C. F., and F. Engelmann (1966), Velocity space diffusion from weak plasma turbulence in a magnetic field, *Phys. Fluids, 9*, 2377-2389, doi:10.1063/1.1761629.

Kurth, W. S., G. B. Hospodarsky, D. L. Kirchner, B. T. Mokrzycki, T. F. Averkamp, W. T. Robison, C. W. Piker, M. Sampl, and P. Zarka (2017), The Juno Waves Investigation, *Space Sci. Rev., 213*, 1-4, 347-392, doi:10.1007/s11214-017-0396-y.

Kurth, W. S., and Piker C. W. (2022a), JUNO E/J/S/SS WAVES CALIBRATED SURVEY FULL RESOLUTION V2.0, JNO-E/J/SS-WAV-3-CDR-SRVFULL-V2.0 [Dataset], *NASA Planetary Data System*, doi:10.17189/1520498.

Kurth, W. S., and Piker C. W. (2022b), JUNO E/J/S/SS WAVES CALIBRATED BURST FULL RESOLUTION V2.0, JNO-E/J/SS-WAV-3-CDR-BSTFULL-V2.0 [Dataset], *NASA Planetary Data System*, doi:10.17189/1522461.

Li, W., Thorne, R. M., Angelopoulos, V., Bonnell, J. W., McFadden, J. P., Carlson, C. W., LeContel, O., Roux, A., Glassmeier, K. H., and Auster, H. U. (2009a), Evaluation of whistler-mode chorus intensification on the nightside during an injection event observed on the THEMIS spacecraft, *J. Geophys. Res., 114*, A00C14, doi:10.1029/2008JA013554.

Li, W., R. M. Thorne, V. Angelopoulos, J. Bortnik, C. M. Cully, B. Ni, O. LeContel, A. Roux, U. Auster, and W. Magnes (2009b), Global distribution of whistler-mode chorus waves observed on the THEMIS spacecraft, *Geophys. Res. Lett., 36*, L09104, doi:10.1029/2009GL037595.

Li, W., R. M. Thorne, J. Bortnik, Y. Y. Shprits, Y. Nishimura, V. Angelopoulos, C. Chaston, O. Le Contel, and J. W. Bonnell (2011), Typical properties of rising and falling tone chorus waves, *Geophys. Res. Lett., 38*, L14103, doi:10.1029/2011GL047925.

Li, W., Q. Ma, R. M. Thorne, J. Bortnik, C. A. Kletzing, W. S. Kurth, G. B. Hospodarsky, and Y. Nishimura (2015), Statistical properties of plasmaspheric hiss derived from Van Allen Probes data and their effects on radiation belt electron dynamics. *J. Geophys. Res. Space Physics, 120*, 3393-3405. doi: 10.1002/2015JA021048.

Li, W., Thorne, R. M., Ma, Q., Zhang, X.-J., Gladstone, G. R., Hue, V., … Bolton, S. J. (2017). Understanding the origin of Jupiter's diffuse aurora using Juno's first perijove observations. *Geophysical Research Letters, 44*, 10,162- 10,170. https://doi.org/10.1002/2017GL075545.

Li, W., Shen, X.-C., Menietti, J. D., Ma, Q., Zhang, X.-J., Kurth, W. S., & Hospodarsky, G. B. (2020). Global Distribution of Whistler Mode Waves in Jovian Inner Magnetosphere.

Geophysical Research Letters, 47, e2020GL088198. https://doi.org/10.1029/2020GL088198.

Li, W., Ma, Q., Shen, X.-C., Zhang, X.-J., Mauk, B. H., Clark, G., et al. (2021). Quantification of diffuse auroral electron precipitation driven by whistler mode waves at Jupiter. *Geophysical Research Letters, 48*, e2021GL095457. https://doi.org/10.1029/2021GL095457.

Li, L., Omura, Y., Zhou, X.-Z., Zong, Q.-G., Rankin, R., Yue, C., et al. (2023). Chorus wave generation modulated by field line resonance and mirror-mode ULF waves. *Journal of Geophysical Research: Space Physics, 128*, e2022JA031127. https://doi.org/10.1029/2022JA031127.

Ma, Q., Li, W., Chen, L., Thorne, R. M., and Angelopoulos, V. (2014a), Magnetosonic wave excitation by ion ring distributions in the Earth's inner magnetosphere, *J. Geophys. Res. Space Physics, 119*, 844- 852, doi:10.1002/2013JA019591.

Ma, Q., W. Li, L. Chen, R. M. Thorne, C. A. Kletzing, W. S. Kurth, G. B. Hospodarsky, G. D. Reeves, M. G. Henderson, and H. E. Spence (2014b), The trapping of equatorial magnetosonic waves in the Earth's outer plasmasphere, *Geophys. Res. Lett., 41*, 6307-6313, doi:10.1002/2014GL061414.

Ma, Q., Li, W., Bortnik, J., Thorne, R. M., Chu, X., Ozeke, L. G., et al. (2018). Quantitative evaluation of radial diffusion and local acceleration processes during GEM challenge events. *Journal of Geophysical Research: Space Physics, 123*, 1938- 1952. https://doi.org/10.1002/2017JA025114

Ma, Q., Li, W., Zhang, X.-J., Bagenal, F. (2020a). Energetic electron scattering due to whistler mode chorus waves using realistic magnetic field and density models in Jupiter's magnetosphere. *Journal of Geophysical Research: Space Physics, 125*, e2020JA027968. https://doi.org/10.1029/2020JA027968

Ma, Q., Connor, H. K., Zhang, X.-J., Li, W., Shen, X.-C., Gillespie, D., et al. (2020b). Global survey of plasma sheet electron precipitation due to whistler mode chorus waves in Earth's magnetosphere. *Geophysical Research Letters, 47*, e2020GL088798. https://doi.org/10.1029/2020GL088798

Ma, Q., Li, W., Zhang, X.-J., Shen, X.-C., Daly, A., Bortnik, J., et al. (2021a). Energetic electron distributions near the magnetic equator in the Jovian plasma sheet and outer radiation belt using Juno observations. *Geophysical Research Letters, 48*, e2021GL095833. https://doi.org/10.1029/2021GL095833

Ma, Q., Li, W., Zhang, X. -J., Bortnik, J., Shen, X. -C., Connor, H. K., et al. (2021b). Global survey of electron precipitation due to hiss waves in the Earth’s plasmasphere and plumes. *Journal of Geophysical Research: Space Physics, 126*, e2021JA029644. https://doi.org/10.1029/2021JA029644

Ma, Q., X. Chu, D. Ma, S. Huang, W. Li, J. Bortnik, and X.-C. Shen (2023), Evaluating the performance of empirical models of total electron density and whistler-mode wave amplitude in the Earth’s inner magnetosphere, *Front. Astron. Space Sci.*, 10:1232702, doi: 10.3389/fspas.2023.1232702.

Ma, Q., W. Li, X.-J. Zhang, J. Bortnik, X.-C. Shen, A. Daly, et al. (2024), Dataset for "Generation and Impacts of Whistler-mode Waves during Energetic Electron Injections in Jupiter's Outer Radiation Belt" [Dataset], *figshare*, https://doi.org/10.6084/m9.figshare.25347538.

Mauk, B. H., Williams, D. J., McEntire, R. W., Khurana, K. K., and Roederer, J. G. (1999), Storm-like dynamics of Jupiter's inner and middle magnetosphere, *J. Geophys. Res., 104*(A10), 22759- 22778, doi:10.1029/1999JA900097.

Mauk, B. H., J. T. Clarke, D. Grodent, J. H. Waite Jr., C. P. Paranicas, and D. J. Williams (2002), Transient aurora on Jupiter from injections of magnetospheric electrons, *Nature, 415*, 1003-1005.

Mauk, B. H., D. K. Haggerty, S. E. Jaskulek, C. E. Schlemm, L. E. Brown, S. A. Cooper, R. S. Gurnee, C. M. Hammock, J. R. Hayes, G. C. Ho, J. C. Hutcheson, A. D. Jacques, S. Kerem, C. K. Kim, D.G. Mitchell, K. S. Nelson, C. P. Paranicas, N. Paschalidis, E. Rossano, and M. R. Stokes (2017), The Jupiter Energetic Particle Detector Instrument (JEDI) Investigation for the Juno Mission, *Space Sci Rev.*, doi:10.1007/s11214-013-0025-3.

Mauk, B. H., Haggerty, D. K., Paranicas, C., Clark, G., Kollmann, P., Rymer, A. M., … Valek, P. (2018). Diverse electron and ion acceleration characteristics observed over Jupiter's main aurora. *Geophysical Research Letters, 45*, 1277- 1285. https://doi.org/10.1002/2017GL076901

Mauk, B. H. (2022), JEDI CALIBRATED (CDR) DATA JNO J JED 3 CDR V1.0 [Dataset], *NASA Planetary Data System*, DOI:10.17189/1519713.

McComas, D. J., et al. (2017), The Jovian Auroral Distributions Experiment (JADE) on the Juno Mission to Jupiter, *Space Science Reviews, 213*, 1-4, 547-643, doi:10.1007/s11214-013-9990-9.

Menietti, J. D., Shprits, Y. Y., Horne, R. B., Woodfield, E. E., Hospodarsky, G. B., and Gurnett, D. A. (2012), Chorus, ECH, and Z mode emissions observed at Jupiter and Saturn and possible electron acceleration, *J. Geophys. Res., 117*, A12214, doi:10.1029/2012JA018187.

Menietti, J. D., Groene, J. B., Averkamp, T. F., Horne, R. B., Woodfield, E. E., Shprits, Y. Y., de Soria-Santacruz Pich, M., and Gurnett, D. A. (2016), Survey of whistler mode chorus intensity at Jupiter, *J. Geophys. Res. Space Physics, 121*, 9758- 9770, doi:10.1002/2016JA022969.

Menietti, J. D., Averkamp, T. F., Imai, M., Kurth, W. S., Clark, G. B., Allegrini, F., et al. (2020). Low-latitude whistler-mode and higher-latitude Z-mode emission at Jupiter observed by Juno. *Journal of Geophysical Research: Space Physics, 126*, e2020JA028742. https://doi.org/10.1029/2020JA028742

Menietti, J. D., Averkamp, T. F., Kurth, W. S., Imai, M., Faden, J. B., Hospodarsky, G. B., et al. (2021). Analysis of whistler-mode and Z-mode emission in the Juno primary mission. *Journal of Geophysical Research: Space Physics, 126*, e2021JA029885. https://doi.org/10.1029/2021JA029885

Nénon, Q., Sicard, A., and Bourdarie, S. (2017), A new physical model of the electron radiation belts of Jupiter inside Europa's orbit, *J. Geophys. Res. Space Physics, 122*, 5148- 5167, doi:10.1002/2017JA023893.

Rae, I. J., Murphy, K. R., Watt, C. E. J., Halford, A. J., Mann, I. R., Ozeke, L. G., … Singer, H. J. (2018). The role of localized compressional ultra-low frequency waves in energetic electron precipitation. *Journal of Geophysical Research: Space Physics, 123*, 1900–1914. https://doi.org/10.1002/2017JA024674.

Shprits, Y. Y., Menietti, J. D., Gu, X., Kim, K. C., and Horne, R. B. (2012), Gyroresonant interactions between the radiation belt electrons and whistler mode chorus waves in the radiation environments of Earth, Jupiter, and Saturn: A comparative study, *J. Geophys. Res., 117*, A11216, doi:10.1029/2012JA018031.

Stix, T. H. (1992). Waves in plasmas, *American Institute of Physics*, ISBN 0883188597.

Tao, X., Thorne, R. M., Horne, R. B., Ni, B., Menietti, J. D., Shprits, Y. Y., and Gurnett, D. A. (2011), Importance of plasma injection events for energization of relativistic electrons in the Jovian magnetosphere, *J. Geophys. Res., 116*, A01206, doi:10.1029/2010JA016108.

Teng, S., Tao, X., Xie, Y., Zonca, F., Chen, L., Fang, W. B., & Wang, S. (2017). Analysis of the duration of rising tone chorus elements. *Geophysical Research Letters, 44*, 12,074-12,082. https://doi.org/10.1002/2017GL075824

Tomás, A. T., J. Woch, N. Krupp, A. Lagg, K.-H. Glassmeier, and W. S. Kurth (2004), Energetic electrons in the inner part of the Jovian magnetosphere and their relation to auroral emissions, *J. Geophys. Res., 109*, A06203, doi:10.1029/2004JA010405.

Thorne, R. M. (1983), Microscopic plasma processes in the Jovian magnetosphere, in *Physics of the Jovian Magnetosphere*, edited by A. J. Dessler, pp. 454-488, Cambridge Univ. Press, New York.

Thorne, R.M. and Tsurutani, B.T. (1979), Diffuse Jovian aurora influenced by plasma injection from Io. *Geophys. Res. Lett., 6*: 649-652. doi:10.1029/GL006i008p00649

Thorne, R. M., W. Li, B. Ni, Q. Ma, J. Bortnik, L. Chen, D. N. Baker, H. E. Spence, G. D. Reeves, M. G. Henderson, C. A. Kletzing, W. S. Kurth, G. B. Hospodarsky, J. B. Blake, J. F. Fennell, S. G. Claudepierre, and S. G. Kanekal (2013), Rapid local acceleration of relativistic radiation-belt electrons by magnetospheric chorus, *Nature, 504*, 411-414, doi:10.1038/nature12889.

Wang, K., R. M. Thorne, and R. B. Horne (2008), Origin of Jovian hiss in the extended Io torus, *Geophys. Res. Lett., 35*, L16105, doi:10.1029/2008GL034636.

Woodfield, E. E., R. B. Horne, S. A. Glauert, J.D. Menietti, and Y. Y. Shprits (2013), Electron acceleration at Jupiter: input from cyclotron-resonant interaction with whistler-mode chorus waves, *Ann. Geophys., 31*, 1619-1630, doi:10.5194/angeo-31-1619-2013.

Woodfield, E. E., Horne, R. B., Glauert, S. A., Menietti, J. D., and Shprits, Y. Y. (2014), The origin of Jupiter's outer radiation belt, *J. Geophys. Res. Space Physics, 119*, 3490- 3502, doi:10.1002/2014JA019891.

Xia, Z., L. Chen, L. Dai, S. G. Claudepierre, A. A. Chan, A. R. Soto-Chavez, and G. D. Reeves (2016), Modulation of chorus intensity by ULF waves deep in the inner magnetosphere, *Geophys. Res. Lett., 43*, 9444–9452, doi:10.1002/2016GL070280.

Xiao, F., Thorne, R. M., Gurnett, D. A., and Williams, D. J. (2003), Whistler-mode excitation and electron scattering during an interchange event near Io, *Geophys. Res. Lett., 30*, 1749, doi:10.1029/2003GL017123, 14.

Zhang, X.-J., Chen, L., Artemyev, A. V., Angelopoulos, V., & Liu, X. (2019). Periodic excitation of chorus and ECH waves modulated by ultralow frequency compressions. *Journal of Geophysical Research: Space Physics, 124*, 8535–8550. https://doi.org/10.1029/2019JA027201.

Figures and Captions

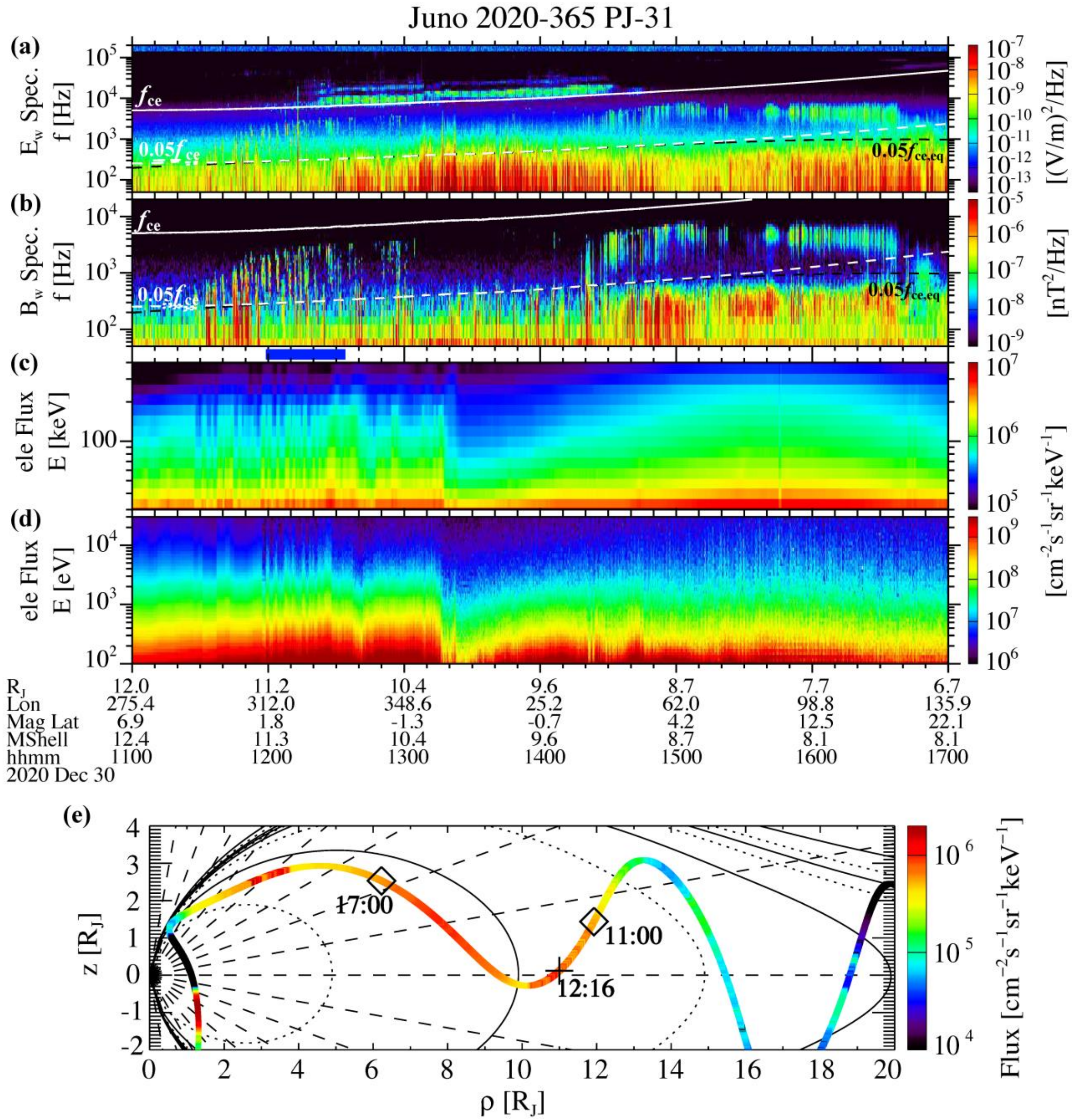

Figure 1. Juno observation of waves and electron fluxes during 11-17 UT on 30 December 2020. (a) Wave electric power spectrogram from 50 Hz to 100 kHz frequencies measured by the Waves instrument; (b) Wave magnetic power spectrogram from 50 Hz to 20 kHz; (c) Spin-averaged electron flux at 30 keV - 400 keV energies observed by JEDI; (d) Spin-averaged electron flux at 0.1 keV - 30 keV energies observed by JADE; (e) ~98 keV electron flux along Juno's trajectory in the polar coordinate system of *M* shell and magnetic latitude. In Panels a-b, the white solid and dashed lines are local electron gyrofrequency (f_{ce}) and 0.05 f_{ce}, respectively, and the black dashed line is $0.05f_{ce,eq}$ ($f_{ce,eq}$ representing the equatorial electron gyrofrequency).

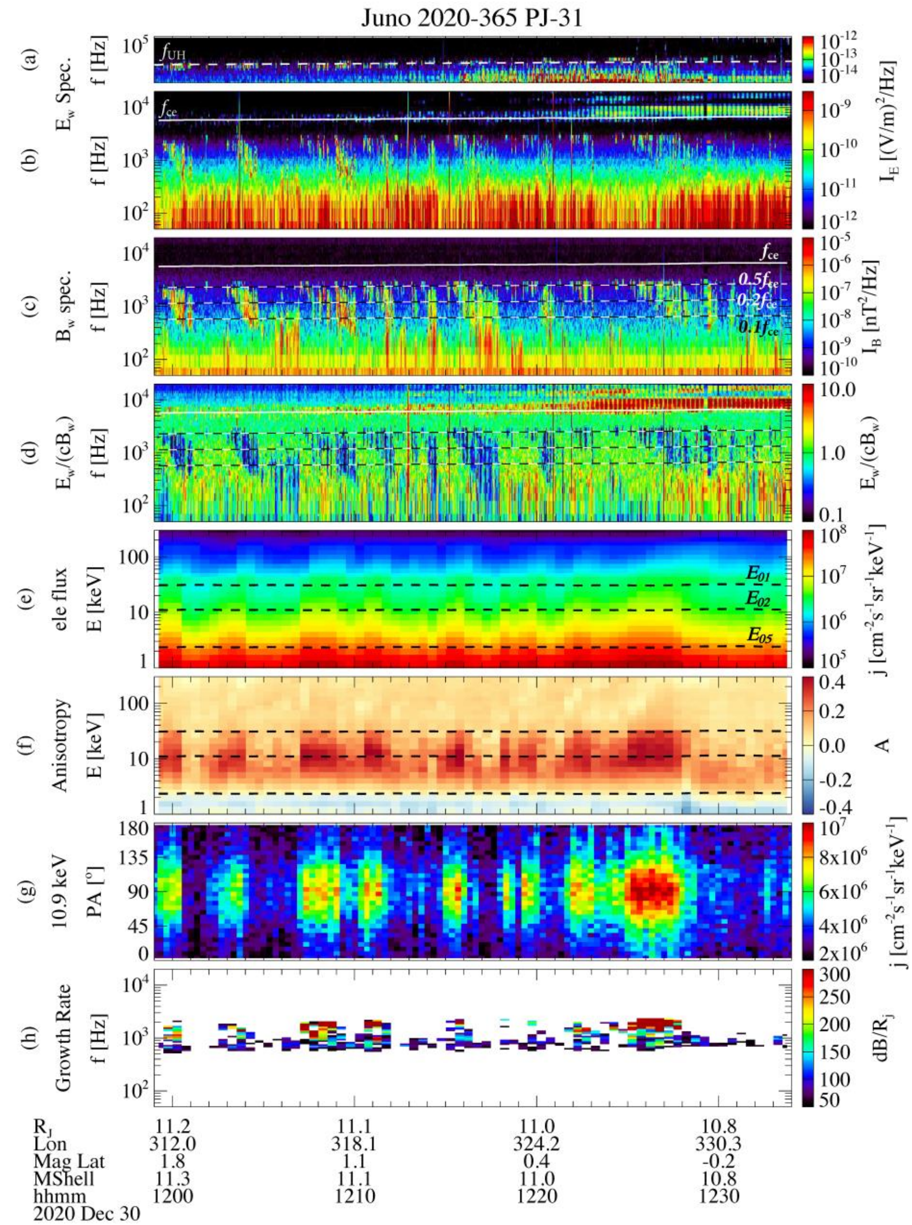

Figure 2. Detailed observation during 11:59 - 12:34 UT on 30 December 2020 and the linear wave growth rate calculation. (a) Wave electric power spectrogram at 20 kHz - 100 kHz frequencies, where the white dashed line is the identified upper hybrid resonance frequency (f_{UH}); (b) Wave electric power spectrogram at 50 Hz - 20 kHz frequencies, where the white solid line is f_{ce}; (c) Wave magnetic power spectrogram at 50 Hz - 20 kHz frequencies, where the white-black dashed lines are 0.1 f_{ce}, 0.2 f_{ce}, and 0.5 f_{ce}, respectively; (d) The ratio of wave electric to magnetic field ($E_w/(cB_w)$); (e) Spin-averaged electron flux at 1 – 300 keV energies, where the black dashed lines are the minimum electron resonance energies (E_{01}, E_{02}, and E_{05}) for parallel-propagating whistler-mode waves at 0.1 f_{ce}, 0.2 f_{ce}, and 0.5 f_{ce} frequencies, respectively; (f) Electron anisotropy calculated from the observed pitch angle distributions; (g) Electron pitch angle distribution at 10.9 keV energy; (h) Frequency spectrogram of wave growth rates calculated using the observed electron distributions.

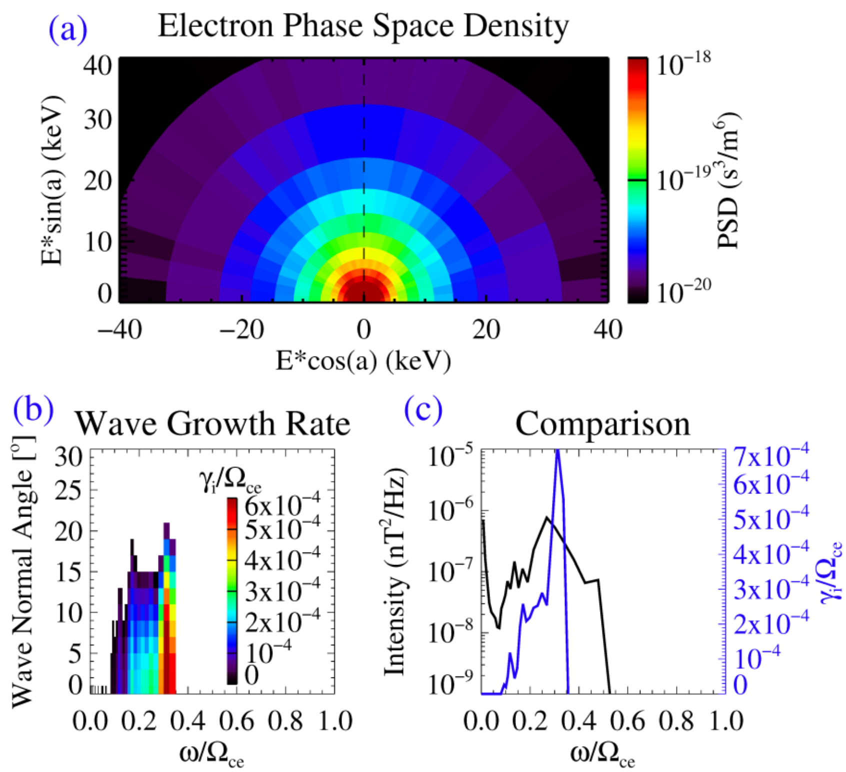

Figure 3. Wave growth rate calculation using the measurements averaged during 12:00 - 12:01 UT. (a) Electron phase space density in the polar coordinate of electron energy and pitch angle; (b) Linear growth rates (γ_i/Ω_{ce}) of whistler-mode waves calculated as a function of wave frequency (ω/Ω_{ce}) and wave normal angle; (c) Comparison between the wave growth rates for 0° wave normal angle (blue) and the measured wave magnetic intensity (black).

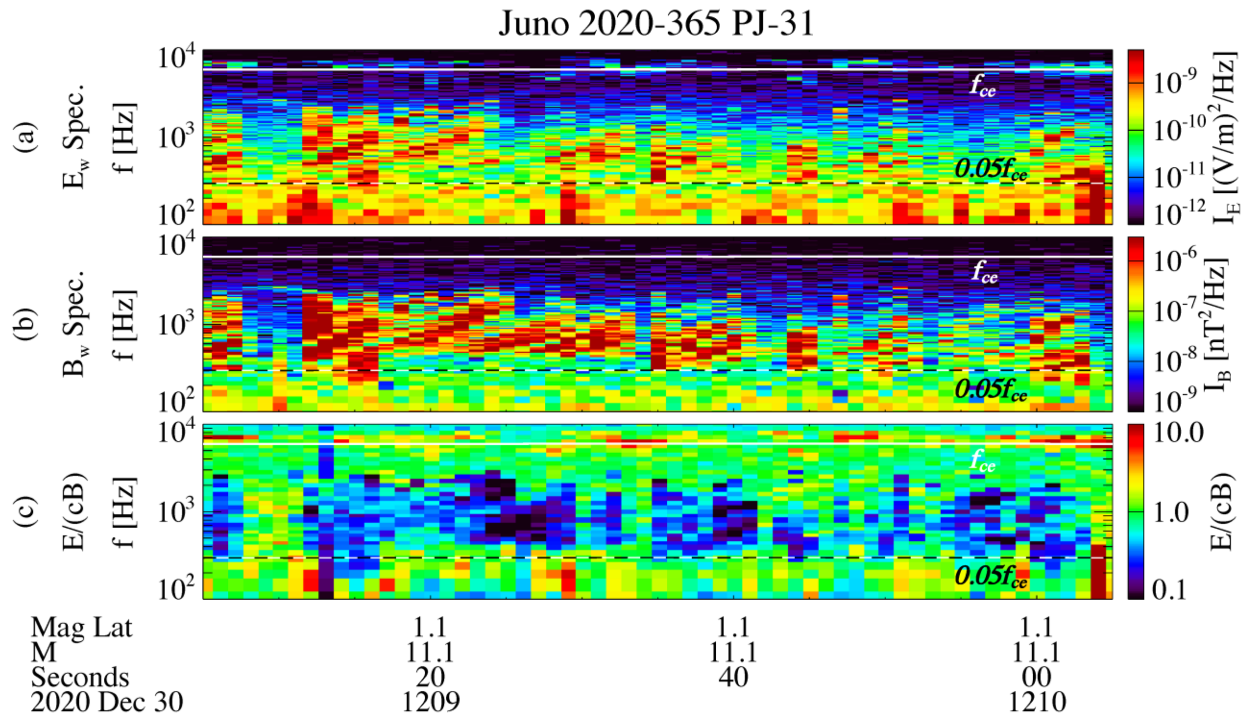

Figure 4. Rising-tone chorus waves observed by the Waves instrument. (a) Wave electric power spectrogram; (b) Wave magnetic power spectrogram; (c) $E_w/(cB_w)$ ratio. The white solid line is f_{ce}, and the white-black dashed line is $0.05f_{ce}$ frequency.

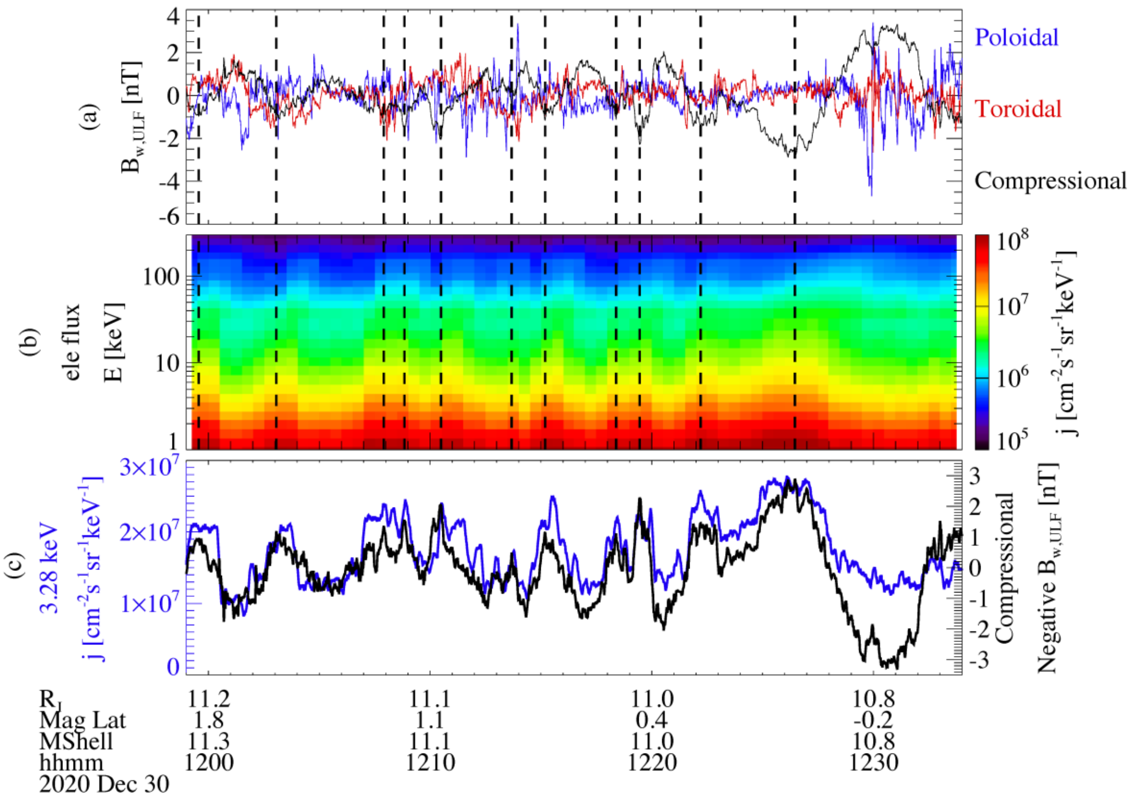

Figure 5. Correlation between ULF waves and electron fluxes observed by Juno. (a) Poloidal (blue), toroidal (red), and compressional (black) components of magnetic field perturbations, obtained after subtracting the total magnetic fields by the smoothed magnetic fields over 10 min in field-aligned coordinates; (b) Spin-averaged electron fluxes measured by JADE and JEDI; (c) Electron flux at 3.28 keV energy averaged in every 10-s time window of JADE measurements (blue), and negative values of the compressional magnetic field perturbations (black). The vertical dashed lines mark the minima of compressional magnetic field perturbations which are correlated with electron fluxes.

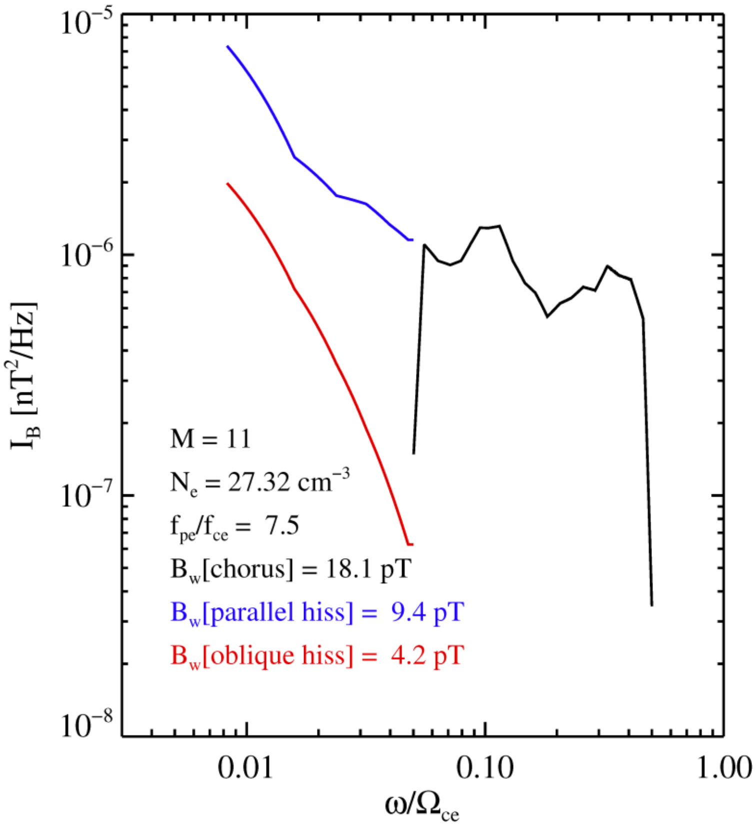

Figure 6. Wave magnetic power spectrum averaged during 11:59 - 12:34 UT. The black, blue, and red lines are the frequency spectra of chorus, quasi-parallel propagating hiss, and oblique propagating hiss waves, respectively. The wave power spectrum and the average parameters as shown are inputs used to calculate the electron diffusion coefficients due to the whistler-mode waves.

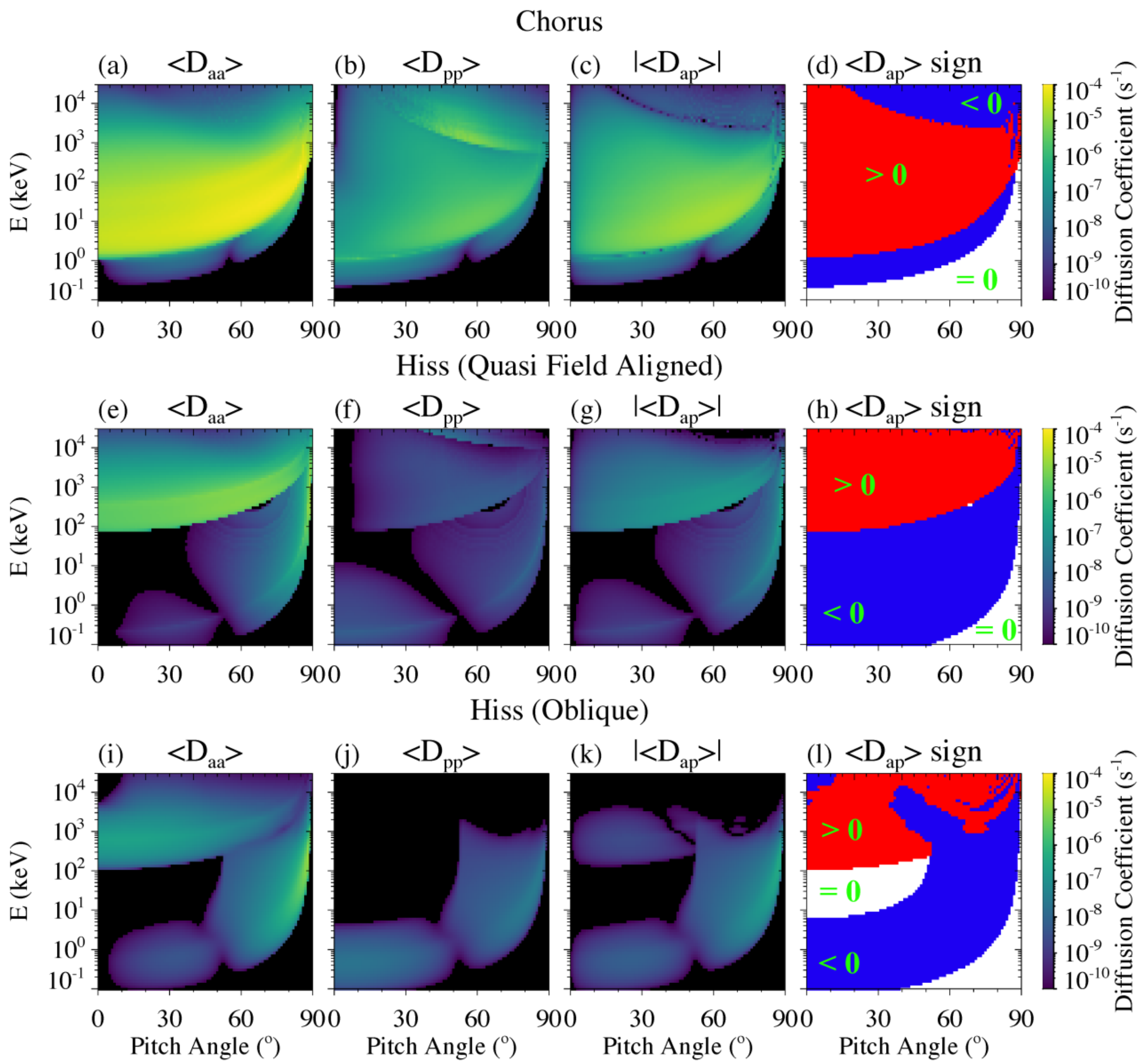

Figure 7. Bounce-averaged pitch angle ($\langle D_{\alpha\alpha}\rangle$), momentum ($\langle D_{pp}\rangle$), absolute value of mixed pitch angle-momentum ($|\langle D_{\alpha p}\rangle|$) diffusion coefficients, and the sign of $\langle D_{\alpha p}\rangle$, due to chorus (a-d), quasi-parallel hiss (e-h), and oblique hiss waves (i-l). The diffusion coefficients are plotted as a function of electron pitch angle at the equator and electron energy. In Panels d, h and l, the red, blue, and white colors indicate positive, negative, and 0 values, respectively.

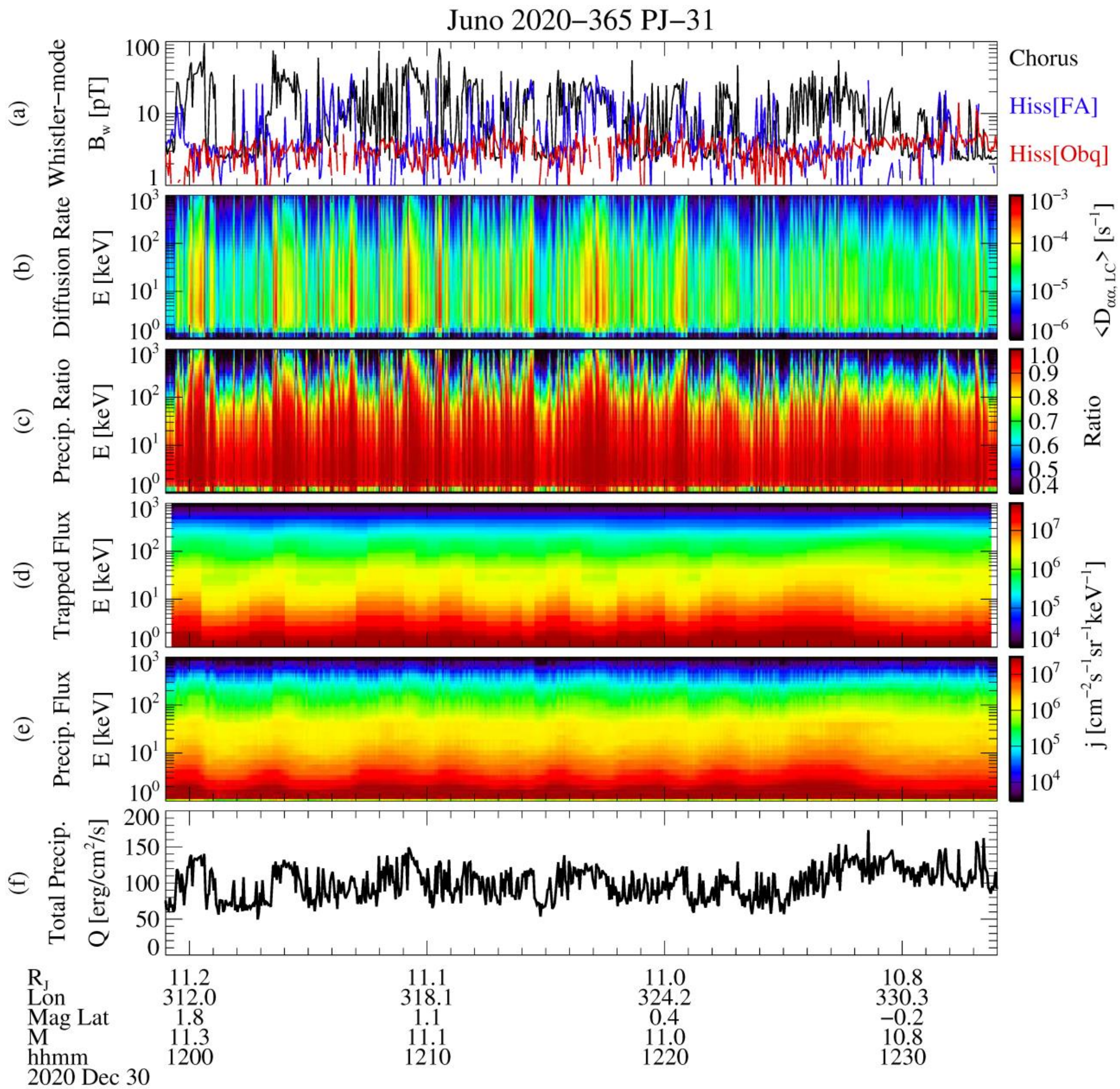

Figure 8. Analysis of electron precipitation due to whistler-mode waves along Juno's trajectory during 11:59 - 12:34 UT on 30 December 2020. (a) Wave magnetic amplitudes of chorus (black), quasi-parallel hiss (blue), and oblique hiss (red) waves; (b) Bounce-averaged pitch angle diffusion coefficients due to the observed whistler-mode waves at the pitch angle of loss cone as a function of electron energy; (c) Electron precipitation ratio, defined as the ratio between average electron flux inside the loss cone and the electron flux just outside the loss cone, calculated using quasilinear theory; (d) The electron flux just outside the loss cone measured by Juno; (e) The modeled precipitating electron flux, which is the average flux inside the loss cone; (f) Total energy flux of precipitating electrons.

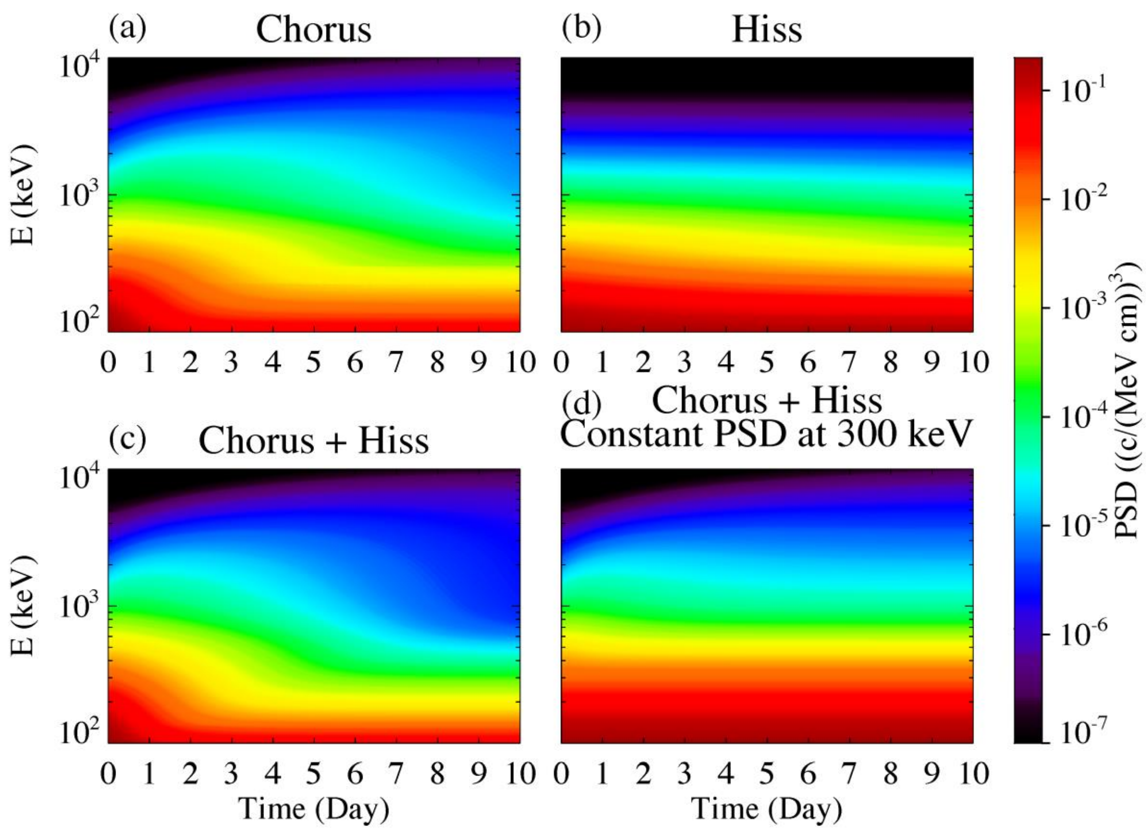

Figure 9. 2D Fokker-Planck simulation of electron phase space density evolution for 10 days at $M = 11$. Spin-averaged phase space density as a function of energy and time due to (a) chorus, (b) quasi-parallel and oblique hiss, (c) both chorus and hiss, and (d) both chorus and hiss but with a constant low energy boundary condition at 300 keV energy.

Figure 1.

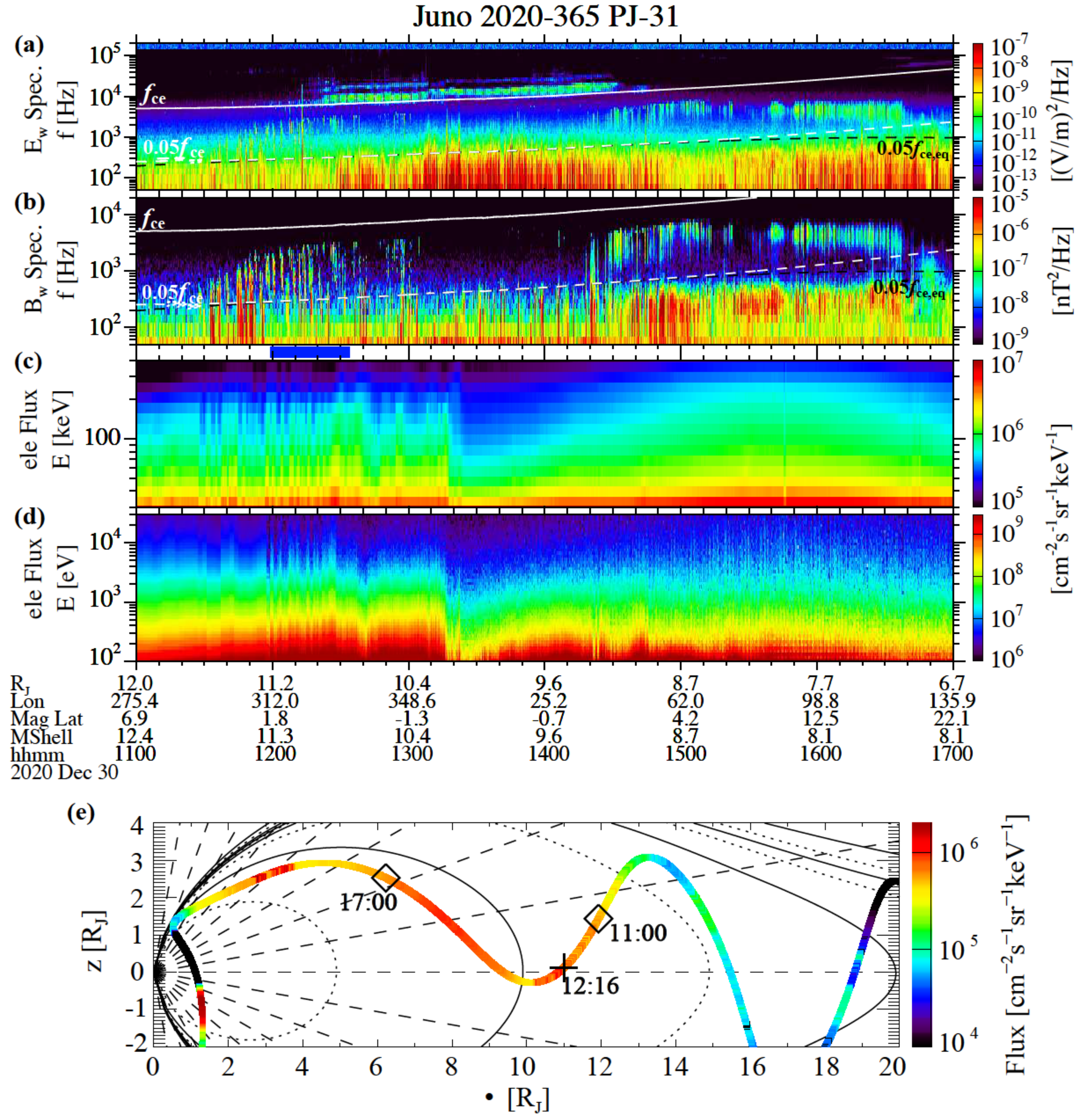

Juno 2020-365 PJ-31
(a)
E_w Spec.
f [Hz]
f_ce
0.05f_ce
0.05f_ce,eq
[(V/m)^2/Hz]
(b)
B_w Spec.
f [Hz]
f_ce
0.05f_ce
0.05f_ce,eq
[nT^2/Hz]
(c)
ele Flux
E [keV]
(d)
ele Flux
E [eV]
[cm^-2s^-1sr^-1keV^-1]
R_J 12.0 11.2 10.4 9.6 8.7 7.7 6.7
Lon 275.4 312.0 348.6 25.2 62.0 98.8 135.9
Mag Lat 6.9 1.8 -1.3 -0.7 4.2 12.5 22.1
MShell 12.4 11.3 10.4 9.6 8.7 8.1 8.1
hhmm 1100 1200 1300 1400 1500 1600 1700
2020 Dec 30
(e)
z [R_J]
17:00
11:00
12:16
• [R_J]
Flux [cm^-2s^-1sr^-1keV^-1]

Figure 2.

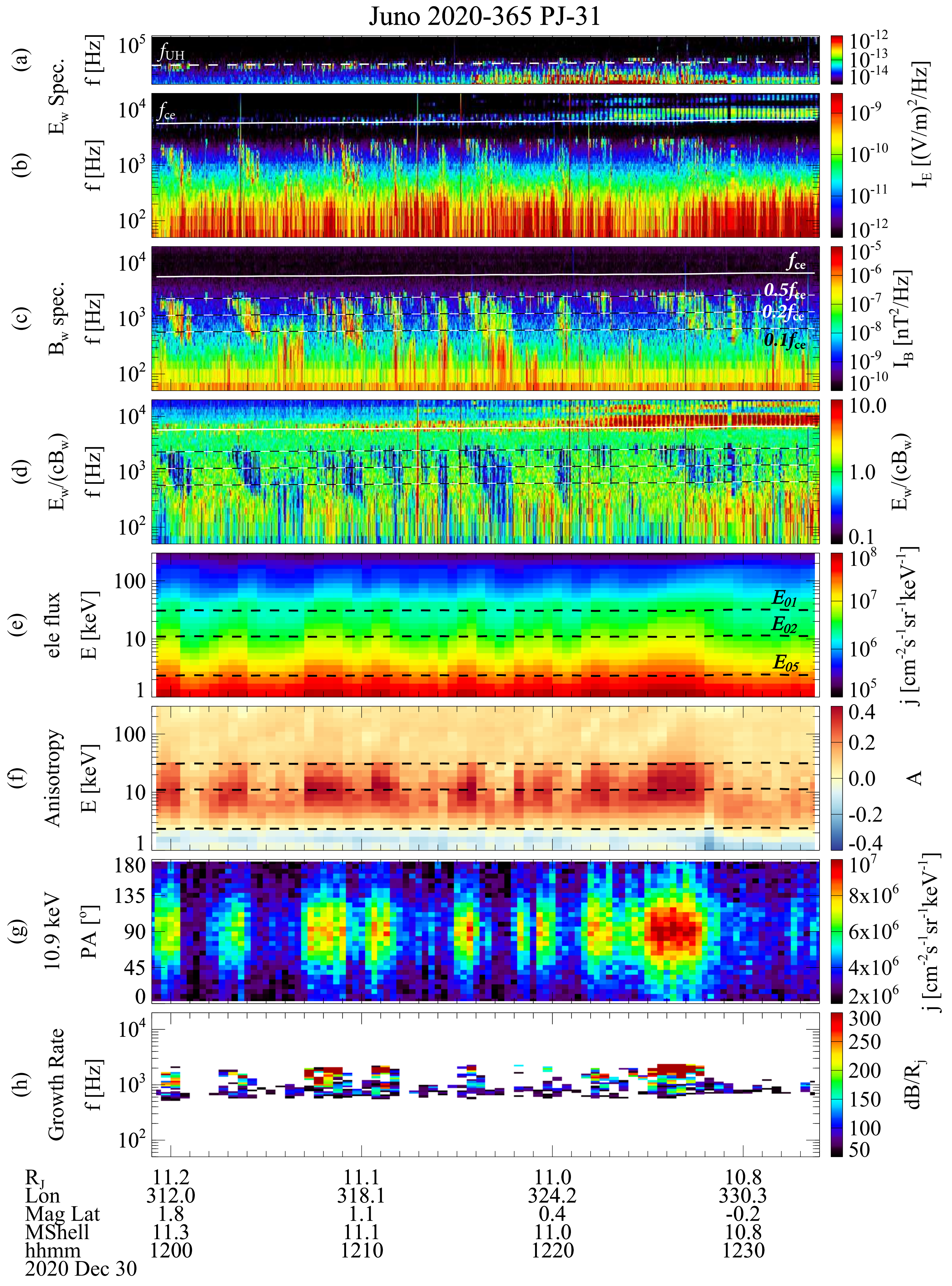

Juno 2020-365 PJ-31
(a) (b) E_w Spec.
(c) B_w spec.
(d) $E_w/(cB_w)$
(e) ele flux
(f) Anisotropy
(g) 10.9 keV
(h) Growth Rate
f [Hz]
E [keV]
PA [°]
f_{UH}
f_{ce}
$0.5f_{ce}$
$0.2f_{ce}$
$0.1f_{ce}$
E_{01}
E_{02}
E_{05}
I_E [(V/m)^2/Hz]
I_B [nT^2/Hz]
$E_w/(cB_w)$
j [cm^{-2}s^{-1}sr^{-1}keV^{-1}]
A
dB/R_j
R_J 11.2 11.1 11.0 10.8
Lon 312.0 318.1 324.2 330.3
Mag Lat 1.8 1.1 0.4 -0.2
MShell 11.3 11.1 11.0 10.8
hhmm 1200 1210 1220 1230
2020 Dec 30

Figure 3.

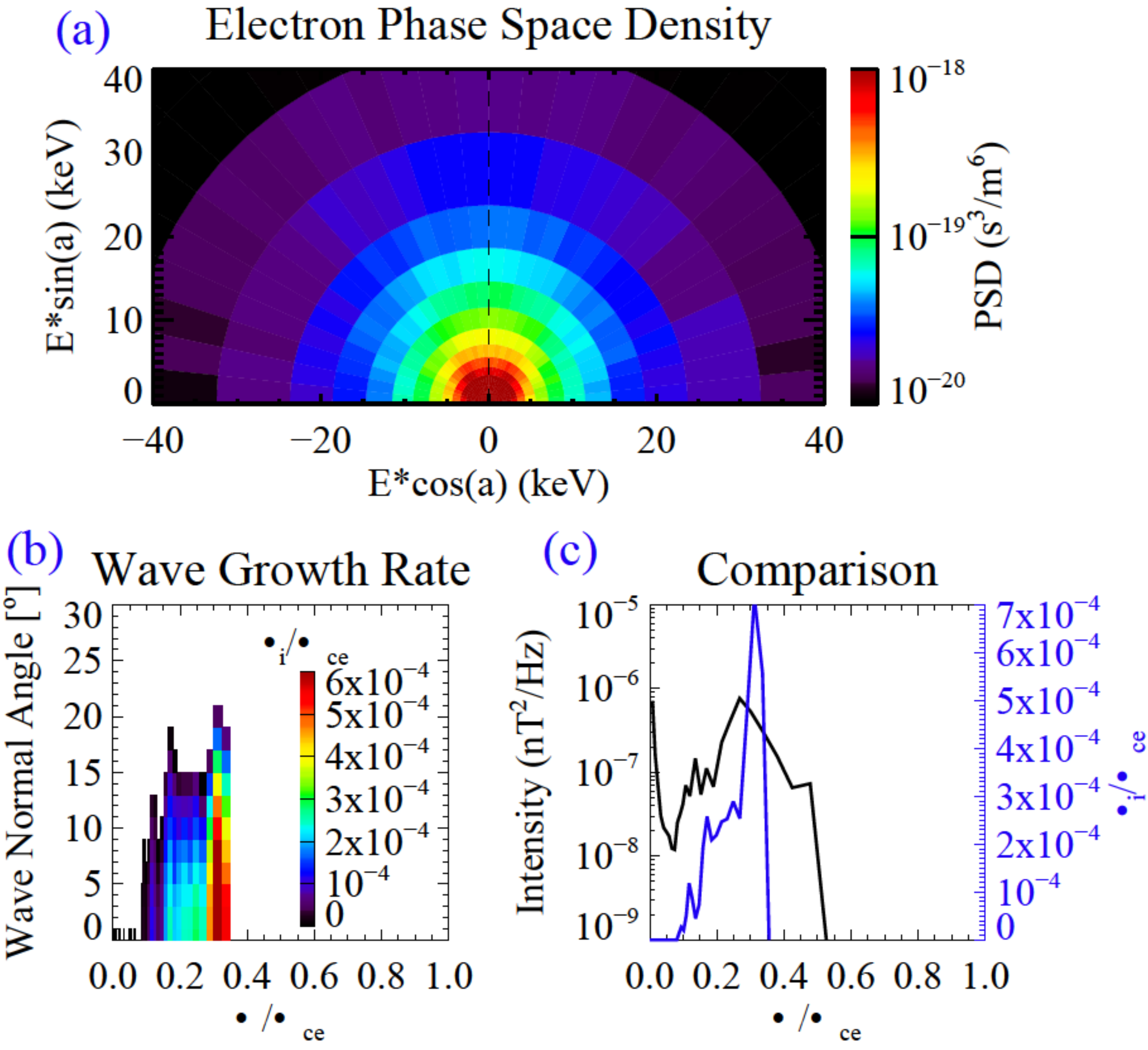

(a)
Electron Phase Space Density
E*sin(a) (keV)
E*cos(a) (keV)
PSD (s^3/m^6)
(b)
Wave Growth Rate
Wave Normal Angle [°]
(c)
Comparison
Intensity (nT^2/Hz)

Figure 4.

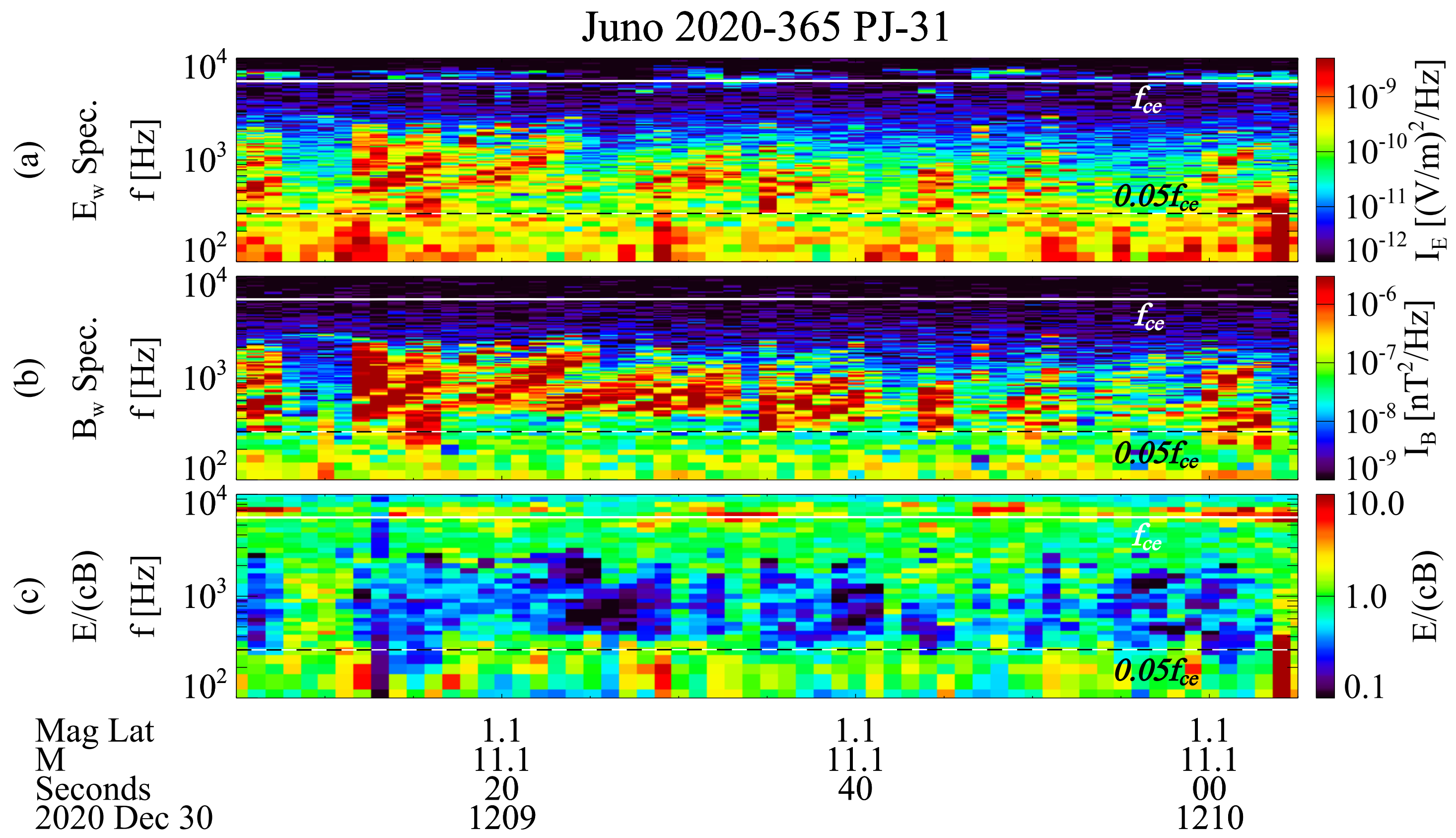

Juno 2020-365 PJ-31
(a) E_w Spec.
f [Hz]
10^4
10^3
10^2
f_{ce}
$0.05f_{ce}$
10^{-9}
10^{-10}
10^{-11}
10^{-12}
I_E [(V/m)^2/Hz]
(b) B_w Spec.
f [Hz]
10^{-6}
10^{-7}
10^{-8}
10^{-9}
I_B [nT^2/Hz]
(c) E/(cB)
f [Hz]
10.0
1.0
0.1
E/(cB)
Mag Lat 1.1 1.1 1.1
M 11.1 11.1 11.1
Seconds 20 40 00
2020 Dec 30 1209 1210

Figure 5.

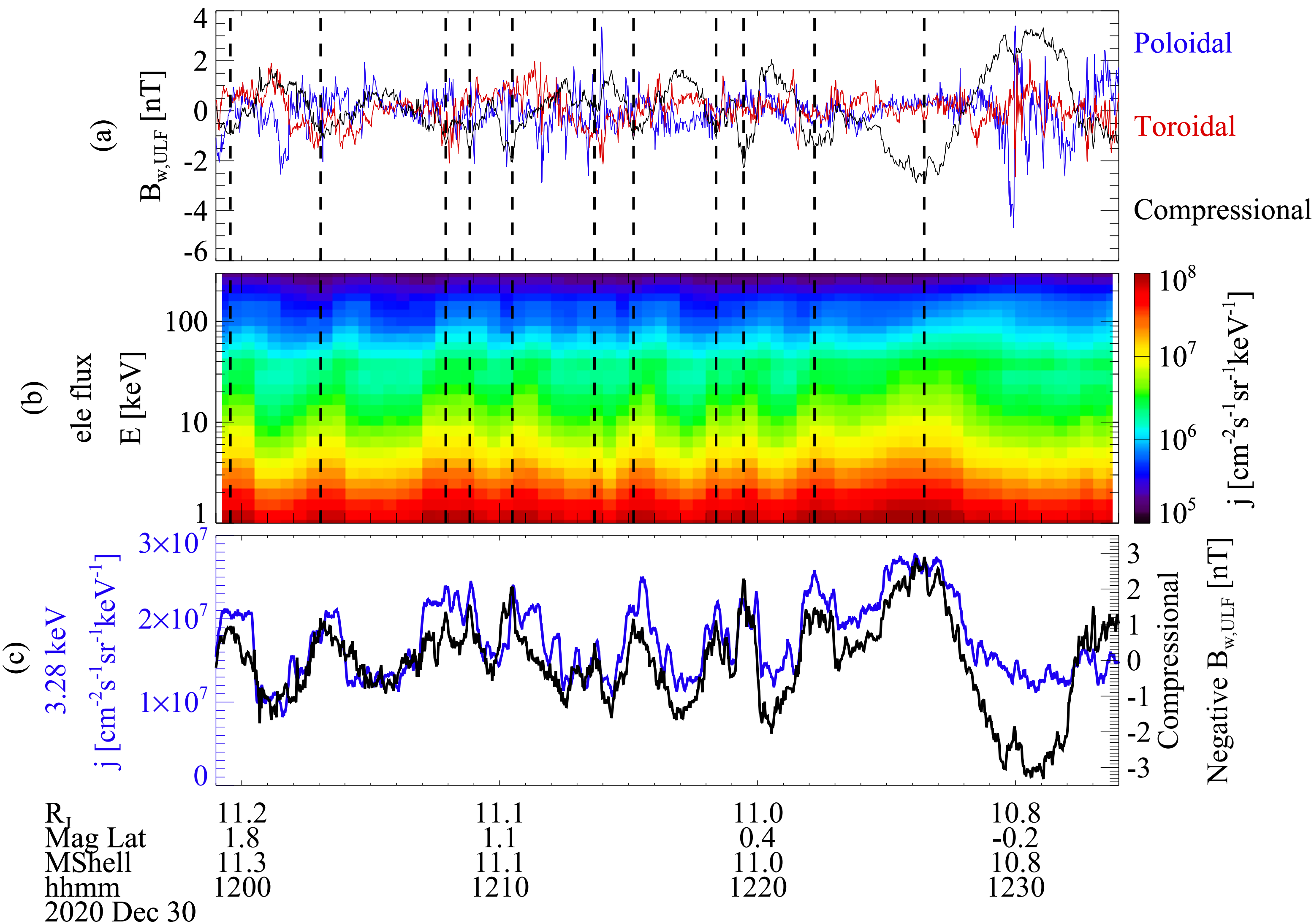

(a)
B_w,ULF [nT]
Poloidal
Toroidal
Compressional
(b)
ele flux
E [keV]
j [cm^-2 s^-1 sr^-1 keV^-1]
(c)
3.28 keV
j [cm^-2 s^-1 sr^-1 keV^-1]
Compressional
Negative B_w,ULF [nT]
R_J 11.2 11.1 11.0 10.8
Mag Lat 1.8 1.1 0.4 -0.2
MShell 11.3 11.1 11.0 10.8
hhmm 1200 1210 1220 1230
2020 Dec 30

Figure 6.

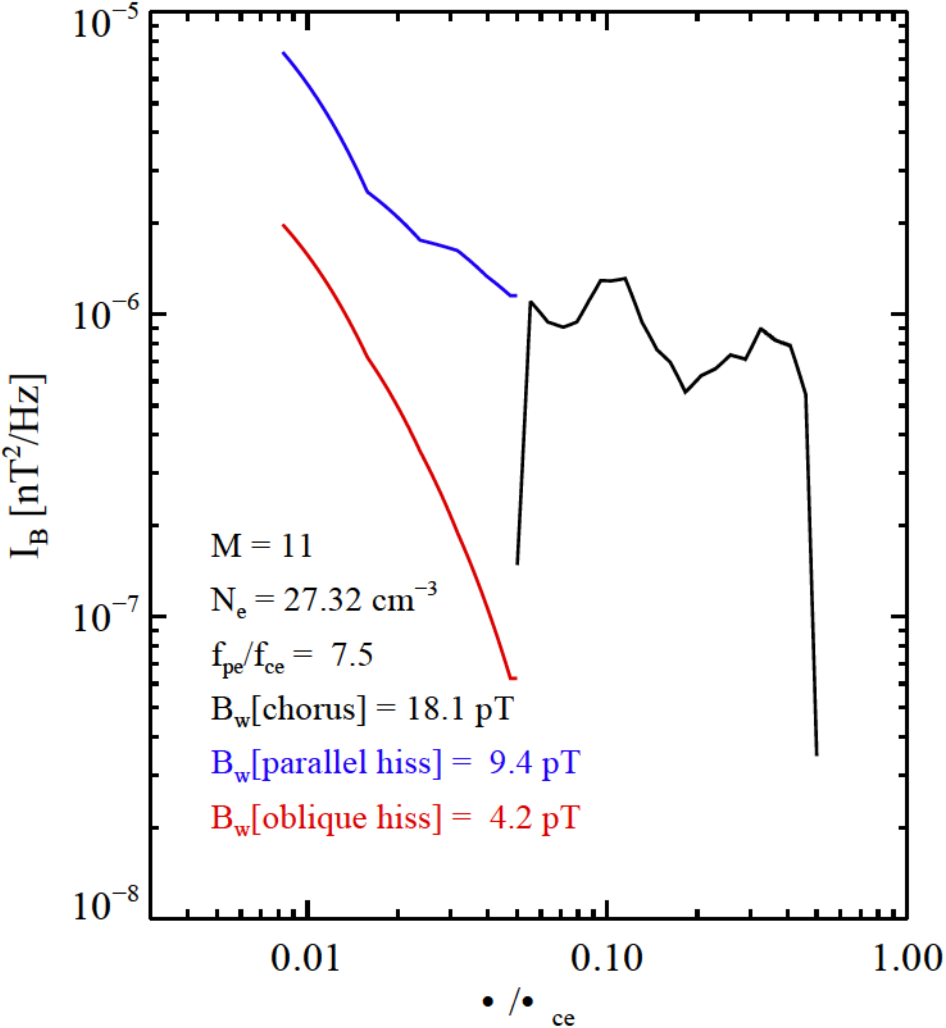

10^{-5}
10^{-6}
10^{-7}
10^{-8}
I_B [nT^2/Hz]
M = 11
N_e = 27.32 cm^{-3}
f_{pe}/f_{ce} = 7.5
B_w[chorus] = 18.1 pT
B_w[parallel hiss] = 9.4 pT
B_w[oblique hiss] = 4.2 pT
0.01
0.10
1.00
• /• ce

Figure 7.

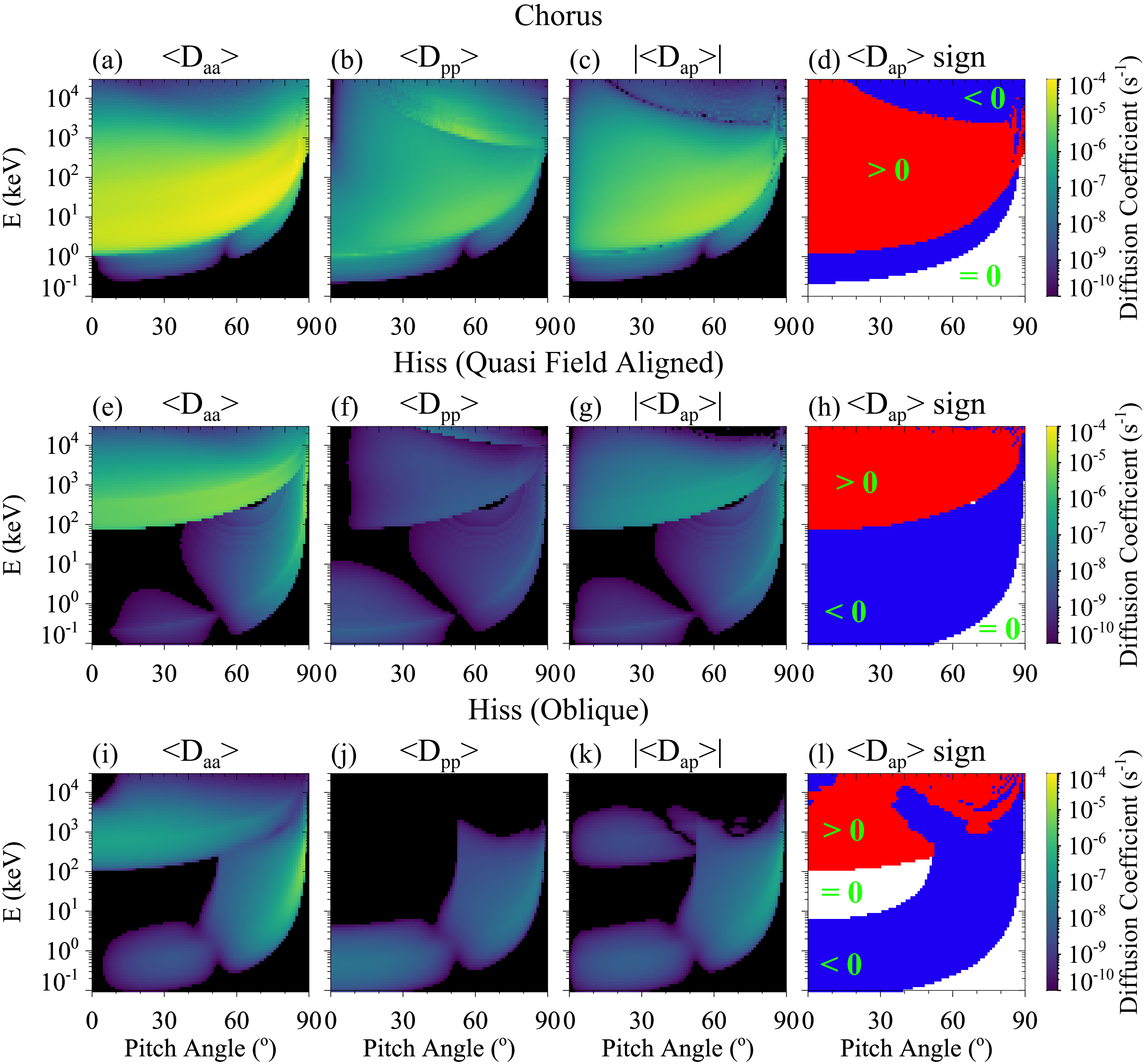

Chorus
(a) <Daa>
(b) <Dpp>
(c) |<Dap>|
(d) <Dap> sign
< 0
> 0
= 0
Hiss (Quasi Field Aligned)
(e) <Daa>
(f) <Dpp>
(g) |<Dap>|
(h) <Dap> sign
> 0
< 0
= 0
Hiss (Oblique)
(i) <Daa>
(j) <Dpp>
(k) |<Dap>|
(l) <Dap> sign
> 0
= 0
< 0
E (keV)
Pitch Angle (o)
Diffusion Coefficient (s-1)

Figure 8.

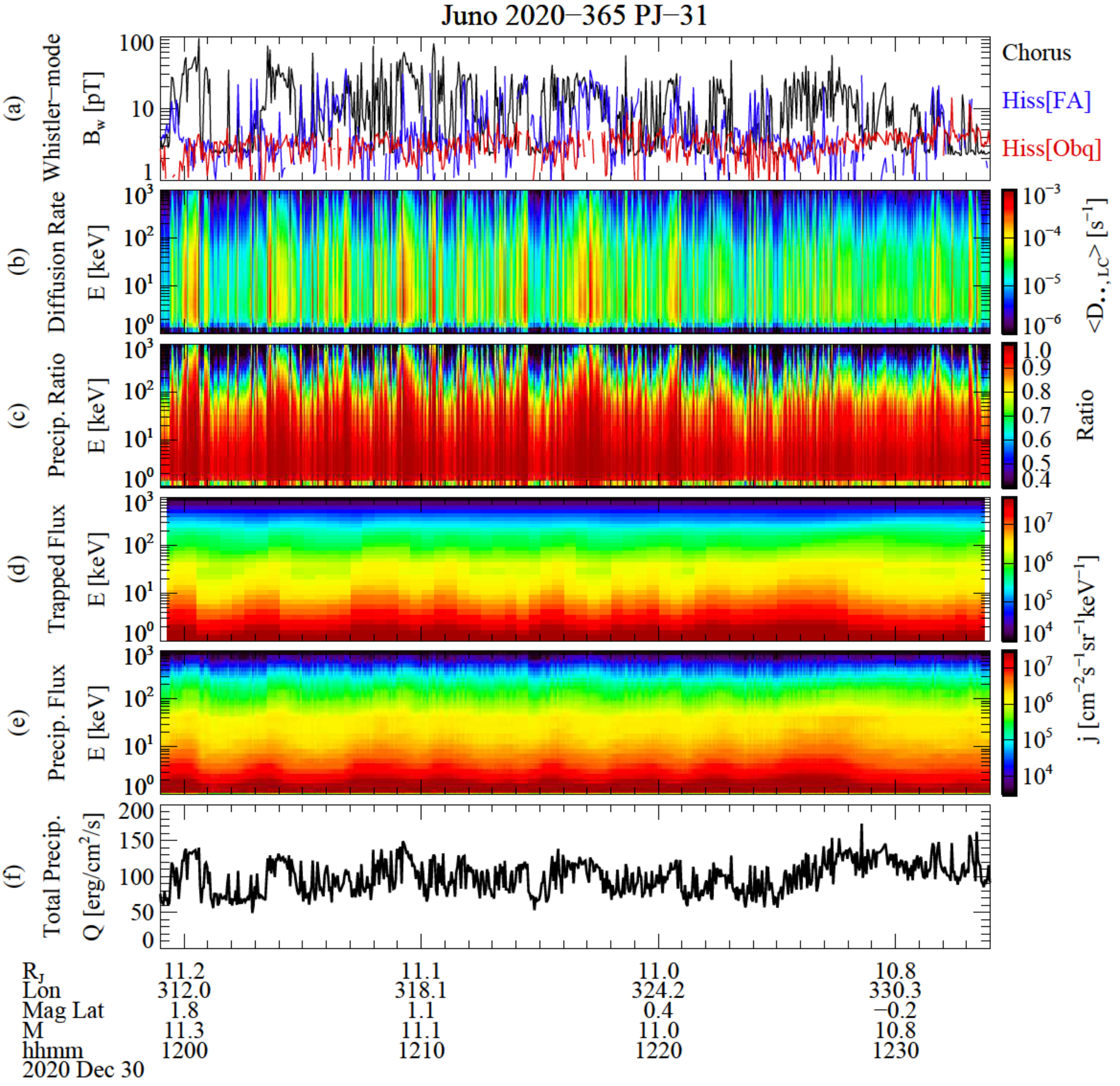

Juno 2020−365 PJ−31
(a) Whistler−mode
B_w [pT]
Chorus
Hiss[FA]
Hiss[Obq]
(b) Diffusion Rate
E [keV]
$<D_{\alpha\alpha,LC}>$ [s^{-1}]
(c) Precip. Ratio
E [keV]
Ratio
(d) Trapped Flux
E [keV]
(e) Precip. Flux
E [keV]
j [$cm^{-2}s^{-1}sr^{-1}keV^{-1}$]
(f) Total Precip.
Q [$erg/cm^2/s$]
R_J 11.2 11.1 11.0 10.8
Lon 312.0 318.1 324.2 330.3
Mag Lat 1.8 1.1 0.4 −0.2
M 11.3 11.1 11.0 10.8
hhmm 1200 1210 1220 1230
2020 Dec 30

Figure 9.

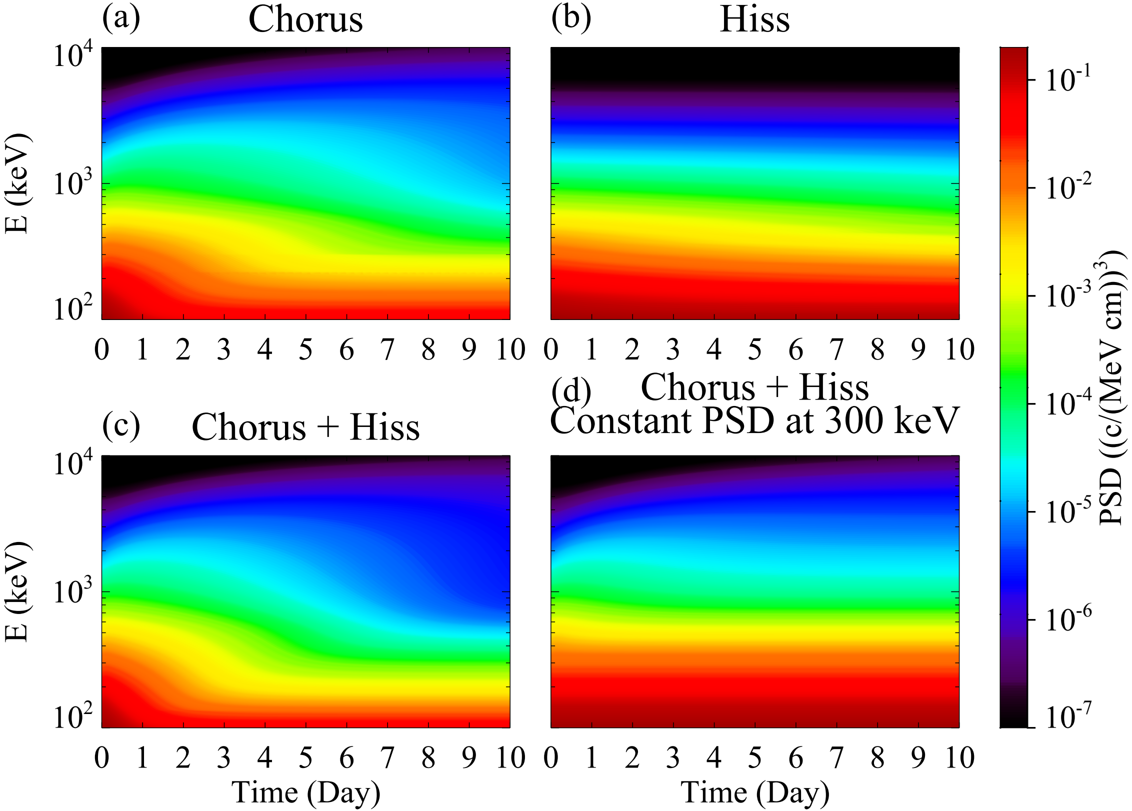
(a) Chorus
(b) Hiss
(c) Chorus + Hiss
(d) Chorus + Hiss
Constant PSD at 300 keV
E (keV)
10^4
10^3
10^2
0 1 2 3 4 5 6 7 8 9 10
Time (Day)
PSD ((c/(MeV cm))^3)
10^{-1}
10^{-2}
10^{-3}
10^{-4}
10^{-5}
10^{-6}
10^{-7}